Thesis for the Degree of Doctor of Philosophy

Multidimensional Constellation Shaping for Coherent Optical Communication Systems

Ali Mirani

CHALMERS

Photonics Laboratory
Department of Microtechnology and Nanoscience - MC2
Chalmers University of Technology
Göteborg, Sweden, 2022

Multidimensional Constellation Shaping for Coherent Optical Communication Systems
Ali Mirani
Göteborg, 2022

ISBN: 978-91-7905-775-6
Doktorsavhandlingar vid Chalmers Tekniska Högskola
Ny serie nr 5241
ISSN 0346-718X

Chalmers University of Technology
Department of Microtechnology and Nanoscience - MC2
Photonics Laboratory
SE-412 96 Göteborg, Sweden
Phone: +46 (0) 31 772 1000

Front cover illustration: Optimum 2-dimensional sphere packing shown in a honeycomb together with a 16-ary constellation.
Credit: weter78/ Shutterstock

Printed in Sweden by
Chalmers Digitaltryck
Chalmers Tekniska Högskola
Göteborg, Sweden, December 2022

Multidimensional Constellation Shaping for Coherent Optical Communication Systems

Ali Mirani
Photonics Laboratory
Department of Microtechnology and Nanoscience - MC2
Chalmers University of Technology

Abstract

To overcome the increasing demands for Internet traffic, exploiting the available degrees of freedom in optical communication systems is necessary. In this thesis, we study how constellation shaping can be achieved in various dimensions and how various shaping schemes affect the whole performance in real systems. This thesis investigates the performance of constellation shaping methods including geometric shaping and probabilistic shaping in coherent fiber-optic systems.

To study geometric shaping, we explore multidimensional lattice-based constellations. These constellations provide a regular structure with fast and low-complexity encoding and decoding. We show the possibility of transmitting and detecting constellations with a size of more than 10^{28} points, which can be done without a look-up table to store the constellation points. Moreover, we experimentally realize our proposed multidimensional modulation formats in long-haul optical communication systems.

Finally, we investigate the performance of probabilistically shaped quadrature amplitude modulation and compare it with uniform cross quadrature amplitude modulation in the presence of transmitter impairments, and with uniform quadrature amplitude modulation in links where higher-order modulation formats co-propagate with on-off keying wavelength channels.

Keywords: optical communications, coherent receiver, constellation shaping, multidimensional modulation format, probabilistic shaping, geometric shaping, lattice-based constellations, Voronoi constellation

Publications

This thesis is based on the work contained in the following papers:

[A] **Ali Mirani**, Erik Agrell, and Magnus Karlsson, "Lattice-based geometric shaping", in *European Conference on Optical Communication (ECOC)*, Brussels, Belgium, Dec 2020.
DOI: 10.1109/ECOC48923.2020.9333162

[B] **Ali Mirani**, Erik Agrell, and Magnus Karlsson, "Low-complexity geometric shaping", *Journal of Lightwave Technology*, vol. 39, no. 2, pp. 363-371, Jan 2021.
DOI: 10.1109/JLT.2020.3033031.

[C] **Ali Mirani**, Kovendhan Vijayan, Shen Li, Zonglong He, Erik Agrell, Jochen Schröder, Peter Andrekson, and Magnus Karlsson, "Physical realizations of multidimensional Voronoi constellations in optical communication systems", submitted to *Journal of Lightwave Technology*, Nov 2022.

[D] Kovendhan Vijayan, **Ali Mirani**, Jochen Schröder, Magnus Karlsson, and Peter Andrekson, "Capacity of phase-sensitively preamplified optical links at low signal-to-noise ratio", in *European Conference on Optical Communication (ECOC)*, Basel, Switzerland, Sep 2022.

[E] **Ali Mirani**, Mikael Mazur, Erik Agrell, Benjamin Foo, Jochen Schröder, Peter Andrekson, and Magnus Karlsson, "Comparison of uniform cross QAM and probabilistically shaped QAM formats under the impact of transmitter impairments", in *European Conference on Optical Communication (ECOC)*, Dublin, Ireland, Sep 2019. DOI: 10.1049/cp.2019.0994

[F] Diego Villafani, **Ali Mirani**, Henrik Åhlfeldt, Jochen Schröder, Magnus Karlsson, and Peter Andrekson, "Performance of probabilistic shaping coherent channels in hybrid systems", in *International Conference on Transparent Optical Networks (ICTON)*, Bari, Italy, July 2020.
DOI: 10.1109/ICTON51198.2020.9203055

Other publications by the author, not included in this thesis, are:

[G] Diego Villafani, **Ali Mirani**, Xiaodan Pang, Edgard Goobar, Jochen Schröder, Magnus Karlsson, and Peter Andrekson, "Phase noise characterization and EEPN of a full C-band tunable laser in coherent optical systems", *IEEE Photonics Technology Letters*, vol. 31, no. 24, pp. 1991-1994, Dec 2019.
DOI: 10.1109/LPT.2019.2952816

[H] Lars Lundberg, Mikael Mazur, **Ali Mirani**, Benjamin Foo, Jochen Schröder, Victor Torres-Company, Magnus Karlsson, and Peter Andrekson, "Phase-coherent lightwave communications with frequency combs", *Nature Communications* 11, 201 (2020).
https://doi.org/10.1038/s41467-019-14010-7.

[I] Shen Li, **Ali Mirani**, Erik Agrell, and Magnus Karlsson, "Designing Voronoi constellations to minimize bit error rate", in *International Symposium on Information Theory (ISIT)*, Melbourne, Australia, Jul 2021.
DOI: 10.1109/ISIT45174.2021.9517815

[J] **Ali Mirani**, Kovendhan Vijayan, Zonglong He, Shen Li, Erik Agrell, Jochen Schröder, Peter Andrekson, and Magnus Karlsson, "Experimental demonstration of 8-dimensional Voronoi constellations with 65,536 and 16,777,216 symbols", in *European Conference on Optical Communications (ECOC)*, Bordeaux, France, Sep 2021.
DOI: 10.1109/ECOC52684.2021.9605988

[K] Shen Li, **Ali Mirani**, Erik Agrell, and Magnus Karlsson, "Low-complexity Voronoi shaping for the Gaussian channel", in *IEEE Transactions on Communications*, vol. 70, no. 2, pp. 865-873, Feb 2022.
DOI: 10.1109/TCOMM.2021.3130286

[L] **Ali Mirani**, Kovendhan Vijayan, Shen Li, Zonglong He, Jochen Schröder, Peter Andrekson, Erik Agrell, and Magnus Karlsson, "Comparison of physical realizations of multidimensional Voronoi constellations in single mode fibers", in *European Conference on Optical Communications (ECOC)*, Basel, Switzerland, Sep 2022.

[M] Rafael Romón Sagredo, Erik Börjeson, **Ali Mirani**, Magnus Karlsso, Per Larsson-Edefors, "Waveform memory for real-time FPGA test of fiber-optic receiver DSPs", in *Nordic Circuits and Systems Conference (NorCAS)*, Oslo, Norway, Oct 2022.
DOI: 10.1109/NorCAS57515.2022.9934184

[N] Shen Li, **Ali Mirani**, Erik Agrell, and Magnus Karlsson, "Power-efficient Voronoi constellations for fiber-optic communication systems", accepted in *Journal of Lightwave Technology*, Nov 2022.
DOI: 10.1109/JLT.2022.3222423

[O] Zexin Chen, Zonglong He, **Ali Mirani**, Jochen Schröder, Peter Andrekson, Magnus Karlsson, Meng Xiang, Yu Yu, Ming Tang, Yuwen Qin, and Songnian Fu, "Transmitter optimization for PS-QAM signal in high spectral efficiency metro-transmission", submitted to *Journal of Lightwave Technology*, Sep 2022.

Contents

Acknowledgement

First and foremost, I would like to thank my supervisor, Prof. Magnus Karlsson, for giving me the opportunity to pursue my Ph.D. in the Photonics group and for sharing all your deep knowledge on optics. I would like to thank my co-supervisor, Prof. Erik Agrell, for all the fruitful discussions and your valuable feedback to improve my writing skills. Special thanks to my examiner, Prof. Peter Andrekson, for managing the lab duties and reminding me of the importance of experimental work.

Dr. Jochen Schröder, Dr. Mikael Mazur, and Dr. Ben Foo deserve special thanks for introducing and helping me with Python programming and sharing your knowledge on fiber-optic communications. Many thanks to Dr. Diego Villafani for the interesting collaborations and discussions in the lab. Special thanks to Dr. Lars Lundberg to involve me in your phase tracking experiment to understand more about optical coherent systems. I wish to thank Dr. Ravikiran Kakarla and Dr. Kovendhan Vijayan for all the friendly discussions and all the experimental knowledge you have taught me. Special thanks to Shen Li for all the collaborations in investigating the Voronoi constellations. I wish to thank Isra, Marcello, Ekaterina, Zonglong, Estrella, and Krishna for your valuable friendship and all the interesting discussions in the lab. Many thanks to Gunnel Berggren for managing all administrative work and being a kind administrator. I would like to thank everyone at the Photonics lab for making it such a nice environment. I would like to thank all my Iranian friends who had made Sweden feel like home.

Last but not least, my deepest thanks go to my parents and my sister for your ever-existed encouragement in all steps of my life and to my partner Maryam for your love and support during the hard days of Ph.D. life.

Ali Mirani
Göteborg, December 2022

Financial support

This work was supported by the Knut and Alice Wallenberg Foundation (KAW), and the Swedish Research Council (VR). Part of the simulations in this work were performed on the resources provided by the Swedish National Infrastructure for Computing (SNIC) at C3SE.

Dedicated to all young Iranians fighting for their freedom

Acronyms

16D	16-dimensional
2D	2-dimensional
4D	4-dimensional
8D	8-dimensional
ADC	analog-to-digital converter
AOM	acousto-optic modulator
APE	asymptotic power efficiency
ASE	amplified spontaneous emission
AWG	arbitrary waveform generator
AWGN	additive white Gaussian noise
B2B	back-to-back
BER	bit-error rate
BICM	bit-interleaved coded modulation
BPF	bandpass filter
BPSK	binary phase-shift keying
CPA	closest point algorithm
DAC	digital-to-analog converter
DP	dual-polarization
DSP	digital signal processing
ECL	external cavity laser
EDFA	erbium-doped fiber amplifier
ENOB	effective number of bits
FEC	forward error correction
FWM	four-wave mixing

GMI	generalized mutual information
GN	Gaussian noise
GS	geometric shaping
HD	hard-decision
IM/DD	intensity modulation with direct detection
IQ	in-phase and quadrature
LSPS	loop-synchronized polarization scrambler
MB	Maxwell-Boltzmann
MI	mutual information
MIMO	multiple-input and multiple-output
ML	maximum likelihood
MLC	multilevel coding
MZM	Mach-Zehnder modulator
NGMI	normalized generalized mutual information
NLSE	nonlinear Schrödinger equation
OOK	on-off keying
OSNR	optical signal to noise ratio
PAS	probabilistic amplitude shaping
PCS	probabilistic constellation shaping
PD	photodetector
PM	polarization-multiplexed
PS	probabilistic shaping
QAM	quadrature amplitude modulation
QPSK	quadrature phase-shift keying
RRC	root-raised-cosine
SD	soft-decision
SDM	space-division multiplexing
SE	spectral efficiency
SER	symbol-error rate
SMF	single-mode fiber
SNR	signal-to-noise ratio
SP	set-partitioning
SPM	self-phase modulation
SSFM	split-step Fourier method
VC	Voronoi constellation
VOA	variable optical attenuator
WDM	wavelength-division multiplexing
WSS	wavelength selective switch
XPM	cross-phase modulation

CHAPTER 1

Introduction

Nowadays, part of the world's education system is carried out online through video streaming platforms [1] and it has become common that institutions offer fully online or hybrid courses. Companies that do not depend on physical interaction and the presence of their employees have shifted to work remotely and have online meetings. People are using social media and video calls more than anytime before. All these online communications have challenged the Internet network to connect people in the whole world together with the best quality possible [2,3], e.g., high bandwidth video streaming. This emphasizes the importance of optical communication systems which are the main backbone and infrastructure of the global Internet network [4]. Without improvements in optical communication systems, the Internet would not have been able to meet the global demands to transmit and access more data.

1.1 History

A starting point for modern optical communication systems dates back to the inventions of lasers [5, 6] and low-loss optical fibers [7] after 1960. The invention of the laser brought the opportunity of utilizing a coherent and monochromatic light source to transmit information. In 1960, the first solid ruby laser was invented by Theodore Maiman [8]. The first continuously operating gas laser was invented [9] by Ali Javan et al.,

at Bell Labs in 1961. In 1962, the first semiconductor diode laser was fabricated [10] by Robert N. Hall and coworkers at the General Electric Research and Development Center. Optical fibers were used during the 1960s for gastroscopy [11] despite high attenuation and a short length. Later, more efforts were made to reduce impurities and reduce the fiber losses from 20 dB/km in 1970 [12] to today's less than 0.2 dB/km at infrared wavelength region near 1.55 μm [7, 13, 14]. Demonstrations of commercial fiber optical transmission during the 1970s to transmit data rates of Mbit/sec over a few kilometers were another huge step for the communication community and industry [15, 16].

Another important breakthrough in optical communication was the invention of the erbium-doped fiber amplifier (EDFA) in the 1980s [17]. The EDFA eliminated the optical-electrical-optical repeaters, by amplifying the signal directly in the optical domain and decreasing the cost and complexity of long-haul transmission links [18]. Moreover, because of the high bandwidth of EDFAs separate wavelength channels could be simultaneously amplified and higher data rates transmitted in the same fiber [19].

Studied in the 1980s, coherent receivers were another milestone for optical communication systems. Because of the hardware complexity, they were forgotten under the shadow of optical amplifiers for almost 20 years [20]. In 2005, a coherent receiver was used to detect a polarization-multiplexed quadrature phase-shift keying (QPSK) signal in a wavelength-division multiplexing (WDM) system followed by digital signal processing (DSP) to improve the sensitivity and phase estimation [21]. This created a widespread interest in coherent optical communication systems again since it brought access to the full optical field to increase the spectral efficiency (SE) by employing multi-level modulation formats [22].

All the previous developments have been responsible to increase the data rate and transmission reach in optical communication systems. One question that remains is the ultimate capacity of the optical fibers. In 1948, Shannon showed that for a linear communication channel with an additive Gaussian noise source, the channel capacity C is determined by the available bandwidth W and the signal-to-noise ratio (SNR) through $C = W \log_2(1 + SNR)$ [23]. However, the optical channel is not an additive white Gaussian noise (AWGN) channel in all operation regimes. For optical channels, many efforts have been made to close the gap between the achievable information rate and the channel capacity in lin-

ear regime [24] and to find an estimate for the actual nonlinear capacity [25–27].

1.2 Thesis overview

The focus of this thesis is on investigating the performance of constellation shaping methods to improve the achievable information rate and power efficiency in coherent optical communication systems. Two main approaches are geometric shaping (GS) [28, 29] and probabilistic shaping (PS) [30, 31], where the geometry and the probability distribution of constellation points are modified to improve the performance compared to quadrature amplitude modulation (QAM) formats, respectively. These methods are mainly designed for the linear AWGN channel and their performance needs to be evaluated over the nonlinear fiber channel.

The papers included in this thesis are investigating these constellation shaping methods. In [Paper A-B], the performance of the lattice-based geometric shaping method is explored in the AWGN and nonlinear fiber channels, and fast and low-complexity modulation and demodulation algorithms are presented. Constellation sizes with more than 10^{28} points are simulated without any look-up tables to store them and more than 38% reach improvement is shown compared to 4-QAM. In [Paper C], physical realizations of multidimensional Voronoi constellations are investigated experimentally and compared over the nonlinear fiber channel. Constellations up to 32 dimensions and spectral efficiencies of 4 bits/symb/dimension-pair are demonstrated. In [Paper D], we study fiber links based on phase-insensitive amplifiers and phase-sensitive amplifiers both in simulation and experiment. The best QAM formats in low signal-to-noise ratio in these links are identified and their performances are quantified. In [Paper E], the performance of probabilistically shaped constellations is compared with the cross-QAM formats in the presence of digital-to-analog converter (DAC) and Mach-Zehnder modulator (MZM) impairments without any digital pre-compensation. We demonstrate that cross-QAM outperforms PS-QAM by a factor of up to 4 in symbol error rate and higher achievable information rates, at the same source entropy and optimal electrical signal powers. Finally, in [Paper F], the probabilistically shaped QAM formats are compared with uniform QAM in hybrid systems where on-off keying (OOK) formats are co-propagating with the higher-order modulation formats.

1.2.1 Thesis outline

The outline of this thesis is as follows. In chapter 2, the basic building blocks of a coherent communication system are introduced including the transmitter and the receiver impairments. Different channel models are presented for the fiber channel and the required signal processing algorithms are discussed to compensate for the transceiver and channel distortions. In chapter 3, the modulation formats with their properties and the possible parameters to compare different formats together are introduced. Chapter 4 discusses the constellation shaping methods including both probabilistic and geometric shaping. In chapter 5, physical realizations of multidimensional modulation formats are discussed over available dimensions in optical communication systems. Finally, in chapter 6, the future outlooks are presented and chapter 7 outlines the main results in the appended papers.

CHAPTER 2

Coherent Fiber-Optic Communication Systems

The developments of the global Internet are mainly due to the improvements in fiber links that connect continents, with more than thousands of kilometers of length [32–34]. Early demonstrations of optical links could carry information at Mbits/sec [35], however, today's networks have Tbits/sec capacity [36]. Multiple technologies including lasers, optical amplifiers, and high-speed electrical transceivers have made coherent optical communication systems the main infrastructure in the long-haul transmission of today. Combined with advanced DSP, coherent systems can achieve high SE [37] and be robust against channel impairments [38]. These benefits have made coherent systems dominant for long-haul networks and they are currently attracting more attention to be used in short-reach networks as well [39].

In this chapter, some of the essential building blocks of a point-to-point coherent communication system are investigated including the transmitter, fiber channel, and receiver.

2.1 Transmitter

In this section, the basic components of optical transmitters are introduced including discrete-time signal processing, transforming discrete-time data to a continuous analog electrical signal, and finally converting the electrical signal to the optical domain. A block diagram of the trans-

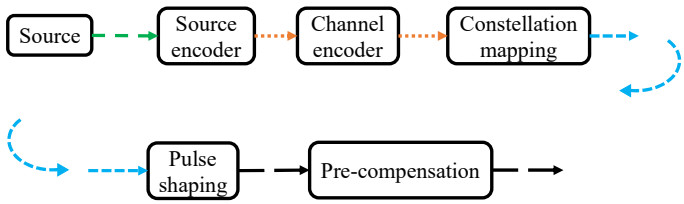

Figure 2.1: The building blocks to transform the source messages to a discrete-time signal. From left to right, different arrows indicate message (green), bit (orange), discrete-time discrete-amplitude (blue), and discrete-time continuous-amplitude (black) information.

mitter side components is given in Fig. 2.1.

2.1.1 Digital domain

As shown in Fig. 2.1, in the first step, source messages are passed through the source encoder to remove the redundant information and generate an efficient bit stream representation. For instance, if the source outputs are the 26 English letters, instead of presenting each letter with 5 bits, it is possible to represent each letter based on their occurrence probability. The letters with higher probability will be presented with fewer bits and the letters with lower probability need more bits. This way, on average, less than 5 bits would be required to show the source outputs [40].

After source coding, the bits are affected by the channel encoding block. The channel coding makes sure that the transmission will be highly reliable by adding redundant bits [41].

The next step after preparing the bits is mapping them to symbols. These symbols are members of a set which is called a *constellation*. There are different ways to represent the symbols, e.g., complex numbers, complex vectors, or multidimensional real vectors [42, 43]. Each symbol $\mathbf{c}$ is labeled by a string of bits as $b_0 b_1 \cdots b_{m-1}$. Then, these symbols are transmitted over their corresponding time slot, polarization, frequency, or spatial mode.

Usually, the combination of channel coding and constellation mapping with an additional shaping block is used to perform constellation shaping either to change the probability distribution or Euclidean geometry of the constellation. More details about constellation shaping are discussed in chapter 4.

In the next step, discrete-time discrete-amplitude symbols $\mathbf{c}$ are car-

ried by a discrete-time continuous-amplitude pulse $h(t)$, i.e.,

$$\mathbf{s}(t) = \sum_i \mathbf{c}_i \cdot h(t - iT), \tag{2.1}$$

where $h(t)$ is the pulse shaping function and i is the time index. Since using square-shaped pulses in the transmission is physically impractical, other forms of pulse shaping are required. In order to satisfy the Nyquist intersymbol interference criterion, usually, the raised cosine pulse shaping is used to transmit the symbols [44, Chap. 7]. To improve noise cancellation, this can also be done by using a root-raised-cosine (RRC) filter in the transmitter and another RRC in the receiver [45, Chap. 9]. Then, the bandwidth of the signal can be controlled by the RRC filter. The transfer function and the time domain impulse response of these filters are given as [46, 47]

$$H_{RC}(f) = \begin{cases} T & : \ 0 \le |f| \le \frac{1-\beta}{2T} \\ \frac{T}{2}\left\{1 + \cos\left[\frac{\pi T}{\beta}\left(|f| - \frac{1-\beta}{2T}\right)\right]\right\} & : \ \frac{1-\beta}{2T} \le |f| \le \frac{1+\beta}{2T} \\ 0 & : \ |f| > \frac{1+\beta}{2T} \end{cases} \tag{2.2}$$

$$h_{RC}(t) = \frac{\sin(\pi t/T)}{\pi t/T} \frac{\cos(\pi \beta t/T)}{1 - 4\beta^2 t^2/T^2} \tag{2.3}$$

$$H_{RRC}(f) = \begin{cases} \sqrt{T} & : \ 0 \le |f| \le \frac{1-\beta}{2T} \\ \sqrt{T}\sin\left(\frac{\pi(1+\beta-2|f|T)}{4\beta}\right) & : \ \frac{1-\beta}{2T} \le |f| \le \frac{1+\beta}{2T} \\ 0 & : \ |f| > \frac{1+\beta}{2T} \end{cases} \tag{2.4}$$

$$h_{RRC}(t) = \frac{2\beta}{\pi\sqrt{T}} \frac{\cos((1+\beta)\pi t/T) + \sin((1-\beta)\pi t/T)\,/\,(4\beta t/T)}{1 - 16\beta^2 t^2/T^2}. \tag{2.5}$$

In these equations, β is the roll-off factor that can control the bandwidth of the filter and it shows the excess bandwidth beyond the Nyquist bandwidth of $1/(2T)$ where T is the symbol duration.

Finally, signal processing can also be done to pre-compensate the chromatic dispersion [48] and/or mitigate the nonlinear response of the fiber [49]. Moreover, the non-ideal transfer function of the transmitter components can be compensated before transferring the data to electrical and optical domains [50]. These non-ideal responses are discussed in the following sections. After pre-compensation, the discrete-time continuous-amplitude signal is ready to be converted to a continuous-time electrical waveform.

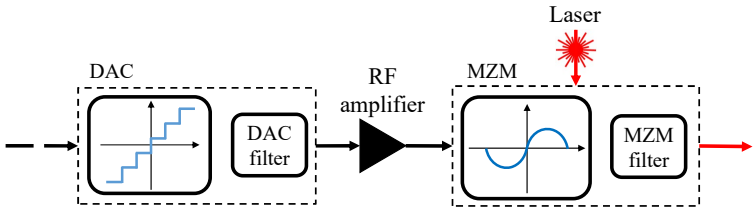

Figure 2.2: The building blocks to transform the discrete-time signal to an optical waveform. The RF amplifier amplifies the electrical signal. From left to right, different arrows indicate a discrete-time signal (dashed black), a continuous-time electrical signal (black), and an optical waveform (red).

2.1.2 Digital-to-analog converter

After the source and channel coding, constellation bit mapping, pulse shaping, and pre-compensation algorithms in the discrete-time domain, the data is ready to be converted to the continuous-time analog electrical domain by the DAC. The DAC is a component that converts the discrete-time signal into a continuous-time analog electrical waveform. It has a finite resolution in terms of discrete output signal levels. A sampling clock and a reference voltage are other essential parts of the DAC [51,52].

Usually, the input to the DAC is normalized between -1 and 1 and the finite resolution of the DAC quantizes the input between specific levels which correspond to the resolution. This can be represented as

$$x = Q(x) + n_q, \tag{2.6}$$

where $Q(\cdot)$ gives the quantized value of the input to the DAC and n_q is called the quantization noise with a uniform distribution whose variance depends on the DAC resolution. The range of each interval which takes the same value at the DAC output is equal to $\Delta = (1-(-1))/2^b = 2^{1-b}$ where b is the DAC resolution. The quantization noise distribution is given by $f(n_q) = (1/\Delta) \cdot \text{rect}(\Delta \cdot n_q)$ where $\text{rect}(\cdot)$ is a rectangular-shaped pulse with unit amplitude and unit domain around 0.

Other DAC impairments are the limited operation bandwidth and electrical noise and jitter. Usually, the DAC frequency response is modeled as a Bessel function [53,54]. These effects reduce the effective number of bits (ENOB) which is used to represent the signal.

2.1.3 Mach-Zehnder modulator

Converting the electrical signal after the DAC to the optical domain is the last step in the transmitter. As shown in Fig. 2.2, the electrical signal at the output of the DAC is amplified by an electrical amplifier to provide enough electrical power. The amplified signal is then fed into an optical modulator which is responsible to change the optical carrier-envelope according to this electrical signal. The optical modulator that is typically used in optical communication systems is the MZM.

An MZM is able to modulate the amplitude of the optical field, however, combining two MZMs with a $\pi/2$ phase-shift in one of the arms enables creating two orthogonal signals in which the amplitude and phase of the optical carrier can be modulated simultaneously. Performing the same procedure over two orthogonal polarization components of the optical carrier provides a four-dimensional space, in which each dimension is controlled and modulated by an MZM [55].

The relation between the output optical power and the input electrical signal of the MZM is described by a sinusoidal function. This nonlinear behavior can distort the signal if the input electrical signal has high power and is not pre-compensated in the digital domain. Usually, in the digital domain, an inverse sinusoidal function is applied to linearize the performance of the overall system [56].

The bandwidth limitation is another non-ideal characteristic of the MZM which is mainly described by a Gaussian filter with a limited bandwidth [57].

2.1.4 Laser

The carrier in the optical communication systems is a light wave that is generated through the process of stimulated emission. The light source at the output of the laser is considered to be more coherent than other light sources in time and space. In coherent communication systems, it is required to have one laser at the transmitter to carry the information signal and one laser at the receiver as the local oscillator to provide the phase reference to detect the relative variations of the received signal. The output of a laser is however not an ideal sinusoidal wave with a well-defined amplitude and phase. Because of the random spontaneous emissions during the process of photon generation, there are random fluctuations in the output power and carrier phase. The single-mode

laser output is then described by a wave amplitude

$$E(t) = (A + \Delta A(t)) \cdot \sin(\omega_0 t + \phi_0 + \Delta\phi(t)), \tag{2.7}$$

where $\Delta A(t)$ and $\Delta\phi(t)$ are the fluctuations of amplitude and phase in continuous time notation, respectively. Also, A, ϕ_0, and ω_0 indicate the amplitude, initial phase, and angular frequency of the light. For simplicity, ϕ_0 is usually considered equal to zero and ΔA is assumed to be negligible because of the feedback control systems. However, the remaining phase perturbations of the received signal are accumulated and result in a phase noise which is described by a Wiener process [58]. In this model, the kth transmitted symbol is affected by a phase rotation of

$$\phi(kT) = \phi((k-1)T) + \theta(kT) = \sum_{m=0}^{k-1} \theta(mT), \tag{2.8}$$

where $\theta(m)$ are independent Gaussian random variables with zero mean and variance $\sigma_\theta^2 = 2\pi\Delta\nu T$, with T indicating the time between the samples and $\Delta\nu$ corresponding to the total transmitter and local oscillator laser linewidths.

The laser linewidth can be measured with different methods. One way is to beat the laser output with a delayed version of itself in a coherent receiver [59]. The delay line is selected to provide uncorrelated phase variations in the detectors and needs to be much larger than the coherence time ($1/\Delta\nu$) of the laser. After detecting the photo-current with a high-speed oscilloscope, signal processing techniques can be used to estimate the laser linewidth. An example setup for this method is shown in Fig. 2.3. In this setup, the laser is split into two arms. The polarization controllers are used to align the polarization states of the fields and an acousto-optic modulator (AOM) shifts the frequency up to avoid low-frequency noise in the spectrum.

2.2 Receiver

As shown in Fig. 2.4, on the receiver side, the inverse operations of the transmitter are applied. First, the optical signal needs to be converted to the electrical domain by the front-end block and then the electrical signal is sampled by the analog-to-digital converter (ADC) to generate the discrete-time signal. Non-ideal responses of the receiver components

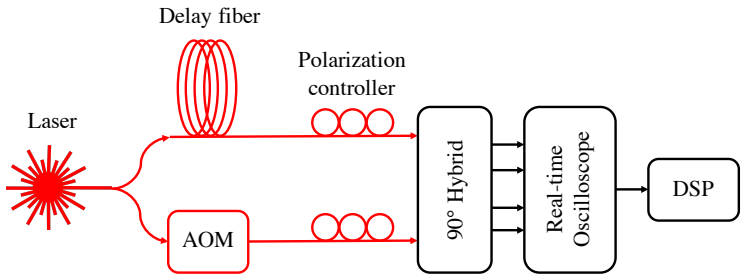

Figure 2.3: Phase noise measurement setup using a coherent receiver. AOM: acousto-optic modulator.

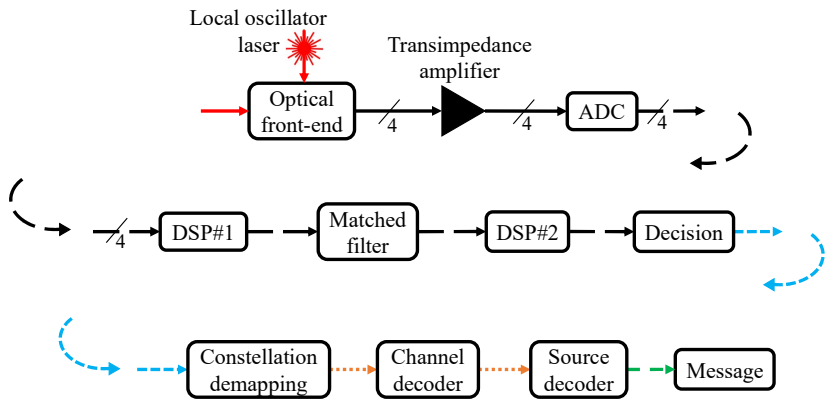

Figure 2.4: Block diagram of the optical receiver. The lines with number indicate 4 real-valued signals.

and some of the fiber impairments, e.g., chromatic dispersion and fiber nonlinearity, can be compensated in the first DSP block. In the next block, matched filtering is applied to improve the SNR of the received signal. Other channel impairments are compensated in the second DSP block and are briefly discussed in this section. Finally, based on the received samples, the most probable transmitted constellation points are selected in the decision block and demapped to generate the corresponding bit stream. In the end, channel decoding is done to correct and find the possible errors and source decoding generates the received messages from the bits.

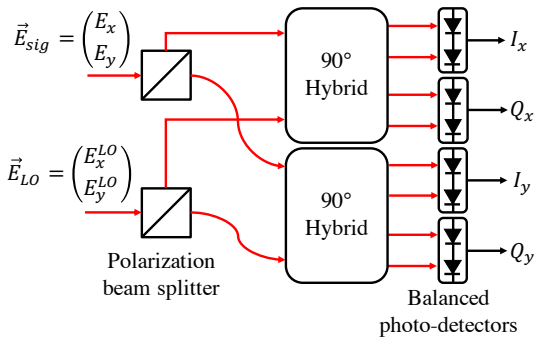

Figure 2.5: Block diagram of a front-end for a dual-polarization system.

2.2.1 Optical front-end

In modern communication systems where phase and amplitude modulations are used together to achieve higher SEs, a coherent receiver is required which consists of a local oscillator as a phase reference. The coherent receiver includes several parts shown in Fig. 2.5. First, the received optical signal and local oscillator are split into two orthogonal polarizations. Then, for each polarization, the signal and local oscillator are mixed in a 90° hybrid. Then, these combined signals are detected by balanced photodetector (PD), which helps to suppress the local oscillator noise and provide larger signal power than single-branch receiver [60, Chap. 2]. Finally, the electrical signal is sampled using an ADC and is ready to be processed in the discrete-time domain.

2.2.2 Digital signal processing

In coherent communication systems, the most important impairments which are compensated in the discrete-time domain are the transceiver components non-ideal responses, fiber channel chromatic dispersion, timing recovery, frequency offset estimation, polarization mixing, phase tracking, and fiber nonlinearities.

Transmitter impairments can be pre-compensated in the digital domain before transmission. However, compensating for these impairments in the receiver side has also been studied which might result in channel noise enhancement compared to the pre-compensation techniques [61]. Coherent receiver impairments can also be mitigated digitally. One famous algorithm which improves the distorted signal because of quadrature imbalance is the Gram-Schmidt orthogonalization [62] procedure

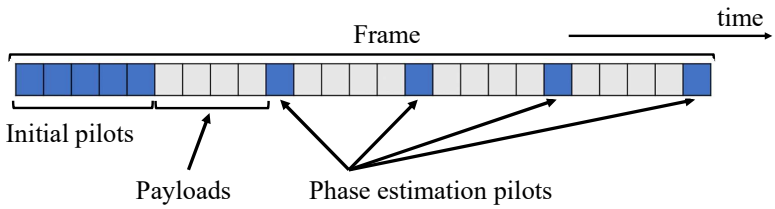

Figure 2.6: Frame structure for pilot-based DSP.

which fixes any potential non-orthogonality of the in-phase and quadrature (IQ) components because of imperfections in hybrids, phase shifters, photodiodes, or even transmitters.

Chromatic dispersion can be compensated either in the optical domain [63] or the digital domain [64]. In the digital domain, the signal passes through an all-pass filter with a response that approximates

$$H(z,\omega) = \exp(j\omega^2\beta_2 z/2), \tag{2.9}$$

or in the time domain

$$h(z,t) = \sqrt{\frac{j}{2\pi\beta_2 z}}\exp(-jt^2/(2\beta_2 z)), \tag{2.10}$$

where β_2 is the group-velocity dispersion parameter, and z is the transmitted distance.

Timing recovery is the recovery of the correct symbol timing, i.e., estimating the optimal time instant to sample in the middle of the signal to capture the received symbols. Garner's feedback algorithm [65] is an example of low complexity time estimation for timing recovery.

In the front-end block, intradyne detection of the received signal by combining with a local oscillator leaves a residual continuous frequency component in the signal. After sampling, this impairment causes a linear phase wander in the received symbols and is usually compensated by removing the data modulation from the signal and finding the highest peak in the Fourier transform of the signal [66].

In order to compensate for polarization mixing and phase tracking, pilot-based DSP has been applied in this thesis. The structure of the pilot symbols and payloads are shown in Fig. 2.6. The pilot symbols are usually selected from a QPSK constellation and are known to the receiver. In the receiver, the received symbols are compared with the known transmitted symbols and their differences are used to estimate

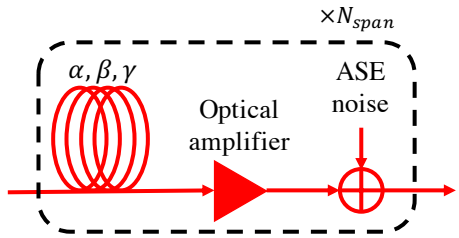

Figure 2.7: Multi-span fiber-optic channel model with inline optical amplification. The N_{span} indicates the number of spans. The fiber length in each span is L and the total propagation distance is $N_{span} \cdot L$.

the channel. Phase pilot symbols are inserted periodically in the frame to track the phase rotations [67].

There are also nonlinear compensation techniques that mitigate the fiber nonlinear effects. Digital backpropagation is one of the methods which has been widely investigated [68]. It is based on the split-step Fourier method (SSFM) and the deterministic effects of the fiber channel which are described by the nonlinear Schrödinger equation (NLSE) are compensated. Drawbacks for this approach are the high computational complexity to solve the NLSE with inverse parameters ($-\alpha$, $-\beta_2$, and $-\gamma$) and the access to the complex signal over the whole bandwidth.

2.3 Fiber-optic channel

In an optical communication system, the main medium in which the light propagates to transfer the signal is the fiber link. The fiber consists of a cylindrical core surrounded by a ring-shaped cladding with a lower refractive index to confine and guide the light through the fiber. The main principle for light propagation inside the fiber is the total internal reflection at the boundary of the core and cladding. Depending on the core diameter, a discrete set of modes can propagate inside the fiber. For a single-mode fiber, the core diameter is usually 5-15μm and the cladding diameter is typically 125μm. To protect the bare fiber, a polymer coating with 250μm diameter is added to cover the cladding. In a single-mode fiber, the core and cladding are made of Silicon dioxide (SiO_2) and they are doped with other materials such as germanium dioxide to change the refractive index [69].

Other types of fibers are coupled or uncoupled multi-core, multi-

mode, and few-mode fibers. Uncoupled multi-core fibers consist of several independent cores inside the cladding which are separated enough to eliminate the coupling between the cores. These fibers can be viewed as parallel single-mode fibers, therefore, conventional transceivers can be utilized. However, due to the separation between the cores, the cladding size might increase which affects the bending stress that they can tolerate. On the other hand, coupled multi-core fibers, provided denser packing of the cores inside the conventional cladding at the expense of coupling between the cores. Therefore, in the receiver, multiple-input and multiple-output (MIMO) signal processing is required. Multi-mode fibers are used in short-reach applications combined with vertical-cavity surface-emitting lasers because of cost and energy efficiencies [70]. Few-mode fibers are similar to multi-mode fibers, however, unlike multi-mode fibers, each mode is modulated with a different signal and they will require MIMO signal processing to compensate for the mode coupling and recover the original signal in the receiver.

Below, some of the fiber impairments which have been considered in this thesis are introduced.

2.3.1 Fiber Losses

The optical power in a fiber decreases as the light propagates across the length. This power loss or attenuation is denoted by α in the units of Np/km. In this unit, the power loss in the fiber is described as

$$\frac{dP}{dz} = -\alpha P, \tag{2.11}$$

where P is the average optical power and z is the propagation distance. For a fiber with length L and input and output optical power of P_{in} and P_{out} the attenuation coefficient in dB/km is

$$\alpha_{[dB/km]} = -\frac{10}{L}\log_{10}\frac{P_{out}}{P_{in}} = -\frac{10}{L}\log_{10} e^{-\alpha L} = 4.343\alpha, \tag{2.12}$$

where in a typical transmission fiber, $\alpha \approx 0.2$ dB/km.

One of the main reasons for fiber losses is the Rayleigh scattering. Randomly located molecules and local fluctuations in the fiber refractive index during manufacture cause the light to scatter in all directions. This intrinsic loss indicates the ultimate loss coefficient for fibers which is proportional to λ^{-4} where λ is the light wavelength. Another loss

Band	Wavelength
O band	1260 nm - 1360 nm
E band	1360 nm - 1460 nm
S band	1460 nm - 1530 nm
C band	1530 nm - 1565 nm
L band	1565 nm - 1625 nm
U band	1625 nm - 1675 nm

Table 2.1: Optical communication wavelength bands.

factor in fiber is the material absorption due to the small impurities such as OH ions [71, Chap. 1].

In a single-mode fiber, the wavelength regions are divided into six bands shown in Table 2.1. Among them, C and L bands are usually used for long-haul communication since their losses are minimized around 0.2 dB/km and amplifiers exist to compensate for the losses.

2.3.2 Chromatic dispersion

The effective index of a mode $n(\omega)$ is not constant over all wavelengths. This wavelength dependency results in different propagation speeds for different frequency components of the signal. In the frequency domain, this corresponds to a phase shift which depends on the propagation distance. Therefore, in a dispersive fiber, the time-domain signal can broaden. This pulse broadening causes inter-symbol interference and limits the minimum pulse duration and the maximum data rate unless it is compensated.

In the wave optics description of light, each fiber mode has a propagation constant $\beta(\omega)$. Taylor expanding β around the angular frequency ω_0 can provide dispersion parameters according to

$$\beta(\omega) = n(\omega)\frac{\omega}{c} = \beta_0 + \beta_1(\omega - \omega_0) + \frac{1}{2}\beta_2(\omega - \omega_0)^2 + \cdots , \qquad (2.13)$$

where c is the speed of light in vacuum and

$$\beta_m = \left(\frac{\mathrm{d}^m \beta}{\mathrm{d}\omega^m}\right)_{\omega=\omega_0}, \quad m = 0, 1, 2, \cdots . \qquad (2.14)$$

In equation (2.13), β_0 and β_1 are propagation constant and inverse group velocity, respectively, and β_2 is known as the *group-velocity dispersion*

parameter and is given in the units of ps^2/km. The dispersion parameter D for the fiber is related to β_2 and is given by

$$D = -\frac{2\pi c}{\lambda^2}\beta_2, \tag{2.15}$$

and usually is reported in the units of ps/(km·nm). Typical values of D in standard fibers are in the range of 15-18 ps/(km·nm) near 1.55 μm.

2.3.3 Fiber Kerr nonlinearities

Due to the very small area of the fiber core, even small optical powers can create very high intensities which can change the properties of fiber including the refractive index. The effective index of a mode, n, is not only a function of frequency ω but also the intensity of light that is propagating inside the fiber, i.e., $n = n(\omega, |E(t)|^2)$ where $E(t)$ is the electric field amplitude in time. This relation causes a phase distortion on the light which depends on the signal power. This phase distortion can be generated from the signal itself (self-phase modulation) or the other signals in a different frequency, polarization, or propagation direction (cross-phase modulation).

2.3.4 Optical amplifiers

In modern long-haul optical communication systems, the optical signal undergoes optical amplification to compensate for fiber losses in the link. Optical amplifiers are a key enabling technology to pave the way for WDM systems. Because of their wide bandwidth, they are able to amplify many wavelength channels simultaneously, directly in the optical domain, which was not possible with the old optical-electrical-optical repeaters.

One of the most widely used optical amplifiers is the erbium-doped fiber amplifier. The fiber inside these amplifiers is doped with the rare-earth element erbium so that it can absorb pump photons in one frequency (980 or 1480 nm) and emit photons at other frequencies through a process known as stimulated emission. Usually, an external laser pumps the high-energy light into the fiber amplifier to excite the erbium atoms. The input signal to the amplifier which can be in the wavelength range of 1530-1620 nm stimulates excited atoms to emit photons at the same wavelength. This procedure amplifies the weak input signal and boosts its power.

However, this amplification is not noiseless. Because of the spontaneous emission of the excited erbium ions, usually, photons with a random phase, frequency, and polarization state rather than the input signal's are generated which reduces the signal quality at the output of the amplifier. These photons are incoherent with the input signal and will be amplified similarly to the input signal. Therefore, this additive noise is called *amplified spontaneous emission (ASE)* noise.

The power spectral density of the ASE noise is given by

$$\rho(\nu) = 2n_{sp}h\nu\left(G(\nu) - 1\right), \tag{2.16}$$

where $G(\nu)$ is optical gain at optical frequency ν, n_{sp} is the spontaneous emission factor, h is the Planck's constant, and the factor of 2 indicates the two orthogonal polarization states. The power of the noise over the bandwidth $B = \nu_{max} - \nu_{min}$ is calculated as

$$P_{ASE} = \int_{\nu_{min}}^{\nu_{max}} \rho(\nu)\mathrm{d}\nu, \tag{2.17}$$

and if the bandwidth is narrow enough to consider a flat power spectral density around ν_0, the noise power is

$$P_{ASE} \approx 2n_{sp}h\nu_0\left(G(\nu_0) - 1\right)B. \tag{2.18}$$

2.3.5 Additive white Gaussian noise channel

A simple approximation for the long-haul optical channels is the AWGN channel. The relation between the input $\mathbf{X}$ and output $\mathbf{Y}$ of this channel is given by

$$\mathbf{Y} = \mathbf{X} + \mathbf{Z} \tag{2.19}$$

where $\mathbf{X}$ and $\mathbf{Y}$ can denote multidimensional vectors. In Fig. 2.1 and 2.4, the input $\mathbf{X}$ indicates data after the constellation mapping block, and output $\mathbf{Y}$ represents the data before decision block. The random vector $\mathbf{Z}$ models the noise and has a multidimensional Gaussian distribution expressed by

$$\mathbf{Z} \sim \mathcal{N}(\mathbf{0}, \mathbf{\Sigma}), \tag{2.20}$$

with a zero mean vector and the covariance matrix of $\mathbf{\Sigma} = \sigma^2\mathbf{I}$ where σ^2 is the noise variance per dimension and $\mathbf{I}$ is the identity matrix [72].

The sources of Gaussian noise for the AWGN approximation of fiber channel are mainly the in-line optical amplifiers with the power given in (2.18).

2.3.6 Nonlinear Schrödinger equation

A detailed model of the lightwave propagation over the fiber link is given by solving Maxwell's equations for a cylindrical waveguide. Under the assumptions of slowly varying envelope, weak higher order nonlinearities and dispersion, instantaneous nonlinear response and low fiber losses, the final differential equation is known as the NLSE [71] described by

$$\frac{\partial E}{\partial z} = -\frac{\alpha}{2}E - i\frac{\beta_2}{2}\frac{\partial^2 E}{\partial t^2} + i\gamma|E|^2 E, \tag{2.21}$$

where $E(z,t)$ is the light pulse envelope at distance z and time t which is measured in a reference frame moving with the pulse at the group velocity $\nu_g = 1/\beta_1$, α is the loss, β_2 is the group velocity dispersion, and γ is the nonlinear coefficient defined as $\gamma = 2\pi n_2/(\lambda A_{\text{eff}})$ with nonlinear Kerr parameter n_2 and the effective mode area A_{eff}. The A_{eff} depends on the mode transverse distribution which is related to the core radius and core-cladding index difference. In Fig. 2.7, $E(0,t)$ and $E(L,t)$ are the input and output of the fiber channel, respectively, where L is the fiber length.

For a dual polarization signal, the NLSE can be extended to the Manakov equations [73, 74]

$$\frac{\partial E_x}{\partial z} = -\frac{\alpha}{2}E_x - i\frac{\beta_2}{2}\frac{\partial^2 E_x}{\partial t^2} + i\frac{8}{9}(|E_x|^2 + |E_y|^2)E_x, \tag{2.22}$$

$$\frac{\partial E_y}{\partial z} = -\frac{\alpha}{2}E_y - i\frac{\beta_2}{2}\frac{\partial^2 E_y}{\partial t^2} + i\frac{8}{9}(|E_x|^2 + |E_y|^2)E_y, \tag{2.23}$$

where $E_x(z,t)$ and $E_y(z,t)$ are the pulse envelopes for two orthogonal polarizations. The factor $8/9$ comes from the averaging due to the random birefringence along the fiber [73].

In order to solve the NLSE or Manakov equations, the SSFM is usually used [71]. This method separates the linear and nonlinear operations in the main partial differential equation and solves them separately in frequency and time domains, respectively, with small step sizes to control the error caused by this splitting. However, using a small step size increases the computational complexity and can make this method very time-consuming [75].

To reduce the complexity of the SSFM, many efforts have been made to approximate the nonlinear fiber channel. Among them, the Gaussian noise (GN) model has been proposed and widely used because of its

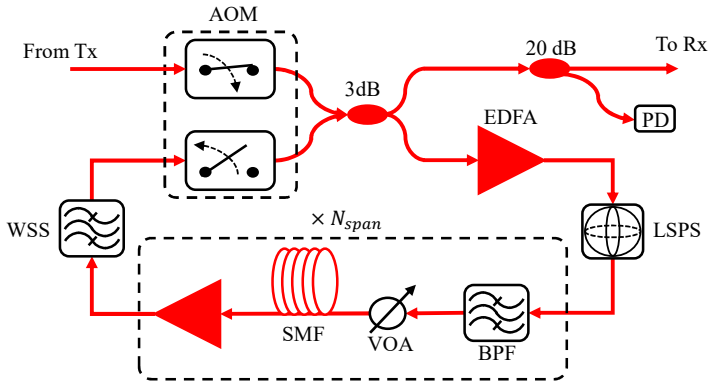

Figure 2.8: Experimental realization of long-haul transmission links using a recirculating loop. Tx and Rx indicate the transmitter and receiver sides, respectively. PD is a low-bandwidth photodetector to monitor the optical power in the loop.

simplicity [76]. This model assumes that the interaction of fiber nonlinearities and chromatic dispersion results in an additive Gaussian noise for the received signal. This model requires a long-haul link without in-line dispersion compensation. During propagation, chromatic dispersion spreads the signal and due to nonlinearity, the signal interacts with itself continuously. According to the central limit theorem, the summation of many independent random variables results in a random variable with a Gaussian distribution which motivated (2.19). It has been shown that the power spectral density of this noise depends on the transmitted signal power via a cubic relationship [77]. Finally, in the receiver, the quality of the signal is reduced due to both the in-line amplifier noise and the additive Gaussian noise of the dispersion and nonlinearity interaction.

2.3.7 Long-haul transmission experiments

Submarine optical links can range from hundreds of kilometers to thousands of kilometers. Investigating the transmission performance over these long-haul links in the lab without a recirculating loop would be very expensive. A recirculating loop consists of an optical loop switch to guide the optical signal in to and out of the loop, a timing control unit, and a few spans of fiber inside the loop. This configuration is shown in Fig. 2.8.

The loop switch consists of two fiber-coupled AOMs, one placed outside the loop to define the loop time and the other one placed inside the

loop to define the recirculating time. Since the AOM introduces a frequency shift (known as the Doppler frequency shift) to the optical signal, either this frequency shift should be compensated [78] or a no-shift AOM device should be used inside the loop. The two AOMs are operating at opposite operation modes, i.e., while one is passing the optical signal, the other one is blocking.

The control unit generates 3 main signals. One signal is sent to the AOMs indicating the loop duration and the recirculating time. A second signal is sent to the loop-synchronized polarization scrambler (LSPS) to scramble the polarization. Finally, the third signal is sent as a trigger signal to the high-speed oscilloscope to capture the signal at a specific round-trip time. These signals are shown in Fig. 2.9 (a), (b), and (c), respectively. A low bandwidth PD is used after the loop to monitor the optical power in each round trip inside the loop. The output signal of the PD is shown in Fig. 2.9 (d). The oscillation in optical power is due to the power variations at the input of the EDFAs due to switching of the AOMs.

Other essential components of a recirculating loop are multiple spans of fiber followed by EDFAs to compensate for the span losses. By increasing the number of spans (N_{span}) inside the loop, fewer round trips are required to achieve a specific transmission distance. Therefore, the optical signal-to-noise ratio (OSNR) reduction due to the loop components, e.g., wavelength selective switch (WSS), AOM, and 3 dB coupler, will be reduced.

Besides the fiber spans and loop switch, an EDFA is required to compensate for the loop component losses, and a LSPS is needed to avoid any accumulated polarization-dependent losses. After the fiber spans and EDFAs, a WSS is used to remove the out-of-band noise and compensate for any gain-tilt due to the cascaded amplifiers in the loop.

(a) Signal to the loop switch

(b) Trigger to the LSPS

(c) Trigger to the receiver

(d) Electrical signal of the PD after the loop

Figure 2.9: RF signals to control and monitor the loop.

CHAPTER 3

Modulation formats

In early optical communication networks, intensity-based modulation formats were dominant because of the low-complexity transmitter and receiver configurations [79]. These noncoherent formats are usually referred to as intensity modulation with direct detection (IM/DD) since they do not require a separate phase reference to be detected and the variation of the light intensity is captured by a PD. Modulation formats that fall in this category are on-off keying and pulse-amplitude modulations. Together with WDM technology, noncoherent formats were able to provide sufficient performance in terms of reach and rate approximately until 2010. However, when even higher data rates were in demand, the SE and sensitivity of these modulation formats became a limiting factor for further improvements.

In order to overcome these limitations, coherent detection in the 4-dimensional (4D) space of light has been developed. Modulating amplitude, phase, polarization, wavelength, time, and spatial mode of the optical signal provide more degrees of freedom to achieve multidimensional modulation formats [80]. By designing modulation formats in multidimensional space, high SEs can be achieved with higher sensitivity than lower dimensionality modulation formats [81, 82].

Today, coherent detection combined with DSP is able to compensate for most of the link impairments digitally rather than using physical hardware [83]. This fact has reduced the hardware implementation

complexity of coherent detection significantly and has made it a preferred solution for long-haul communication links compared to IM/DD approaches, which are used in short-haul and low-cost links. Because of coherent detection, which provides access to higher dimensions of the optical signal, we can design modulation formats to improve their sensitivity and make them more robust to link impairments including the transmitter, receiver, and fiber channel [84, 85].

In this chapter, we introduce the basic definitions for modulation theory including the multidimensional representation. Then, the most common metrics used to compare modulation formats are presented.

3.1 Basic definitions

An intermediate step in a communication link is mapping the binary bits to a set of waveforms, which can modulate a carrier to transmit information over a channel. The coefficients of these waveforms create a multidimensional vector $\mathbf{c}_k$ called a *symbol*. All possible symbols generate a *constellation* $\mathcal{C} = \{\mathbf{c}_0, \mathbf{c}_1, \cdots, \mathbf{c}_{M-1}\}$ with M symbols. The average energy of the constellation is given by

$$E_s = \sum_{i=0}^{M-1} P(\mathbf{c}_i) \left\|\mathbf{c}_i\right\|^2, \tag{3.1}$$

where $P(\mathbf{c}_i)$ is the probability of symbol $\mathbf{c}_i$, $\left\|\mathbf{c}_i\right\|^2$ is the symbol energy and $\|\cdot\|$ is the Euclidean norm of a multidimensional vector. For a constellation with uniform probability distribution, (3.1) is simplified to $E_s = (1/M)\sum_{i=0}^{M-1} \left\|\mathbf{c}_i\right\|^2$.

The constellation entropy is defined as

$$\mathbb{H}(\mathcal{C}) = -\sum_{i=0}^{M-1} P(\mathbf{c}_i) \log_2 P(\mathbf{c}_i), \tag{3.2}$$

which is the average number of bits required to represent one symbol. For constellations with a uniform probability distribution, $\mathbb{H}(\mathcal{C}) = \log_2 M$, and the average energy per bit is $E_b = E_s / \log_2 M$.

Another property of the constellation is the Euclidean distance between the constellation points $d_{ij} = \|\mathbf{c}_i - \mathbf{c}_j\|$, whose minimum value d_{min} gives the performance of the constellation at high SNR.

The geometrical representation of the transmitted information using multidimensional vectors brings us the possibility of looking into denser

packing which—at the same d_{min}—provides reduced constellation energy E_s. This topic is known as *sphere packing* [86].

3.2 Figures of Merit

In this section, we introduce parameters that can be used to compare the properties of modulation formats or their performance over a channel.

3.2.1 Spectral efficiency

For a constellation $\mathcal{C}$ with M symbols in N dimensions and uniform probability distribution, the SE is defined as

$$\beta = \frac{\log_2 M}{N/2}, \tag{3.3}$$

and has the unit of bits per symbol per dimension-pair [87]. This parameter measures the SE for an uncoded transmission system. In fiber-optic communication, usually, a single polarization of light is considered as a pair of dimensions because each polarization can support two IQ components.

Another definition for SE is the transmitted rate over a specific bandwidth.

$$SE = \frac{R_b}{B}, \tag{3.4}$$

where R_b is the channel bit rate, and B the occupied frequency bandwidth of the channel. In this case, the unit is defined as bits per second per Hertz.

3.2.2 Symbol and bit error rate

The symbol-error rate (SER) and bit-error rate (BER) are metrics to show the performance of the transmission over a given channel and denote the probability of errors in received symbols or bits that have happened during the transmission. For probabilistically shaped modulation formats, in order to calculate the SER, the maximum a posteriori decoding rule has been applied in [Paper E], and the symbol decision rule is given in [Paper E, equation (4)]. For equiprobable constellations with maximum likelihood (ML) estimation, using pairwise error probability

and the so-called union bound [45, Chap. 4], the SER in the AWGN channel is bounded from above by

$$\mathrm{SER} \leq \frac{1}{M} \sum_{i=0}^{M-1} \sum_{j \neq i} \frac{1}{2} \mathrm{erfc}\left(\frac{d_{ij}}{2\sqrt{N_0}} \right), \tag{3.5}$$

where $\mathrm{erfc}(x) = (2/\sqrt{\pi}) \int_x^\infty \exp(-t^2) dt$ is the complementary error function and $N_0/2$ is the variance of the Gaussian noise in each dimension. For high SNR, the terms with $d_{ij} = d_{min}$ dominate and the SER is bounded by

$$\mathrm{SER} \lessapprox \frac{\bar{\tau}}{2} \mathrm{erfc}\left(\frac{d_{min}}{2\sqrt{N_0}} \right), \tag{3.6}$$

which $\lessapprox$ means an approximate upper bound that approaches the true value as N_0 goes to zero. Here, $\bar{\tau} = (1/M) \sum_{i=0}^{M-1} \tau_i$, where τ_i is the number of neighbors at the minimum distance from symbol $\mathbf{c}_i$.

The BER depends on the bit labeling of the symbols as well. There are various ways to assign bit labels to constellation points. In this thesis, the focus is on the natural binary and Gray labeling for QAM formats. An example of these two labelings is shown in Fig. 3.1. The SER and BER of QAM formats over the AWGN channel are shown in Fig. 3.2.

3.2.3 Asymptotic power efficiency

For the AWGN channel, at high SNRs, the SER is approximated by the union bound in (3.5) which includes the error probability terms that are based on the minimum Euclidean distance transitions (d_{min}), i.e., $\mathrm{erfc}(d_{min}/(2\sqrt{N_0}))$. Therefore, the high-SNR approximation in (3.5) is a monotonically decreasing function of [42]

$$\frac{d_{min}^2}{4N_0} = \frac{P}{R_b N_0} \gamma = \frac{E_b}{N_0} \gamma, \tag{3.7}$$

where $\gamma = d_{min}^2/(4E_b)$ is defined as the asymptotic power efficiency (APE), E_b is the average energy per bit, R_b is the bit rate, and P is the average transmitted power. The parameter γ depends on the constellation geometry. For binary phase-shift keying (BPSK), QPSK, and dual-polarization (DP) QPSK, the APE is equal to 0 dB. The sensitivity penalty is defined as $1/\gamma$ and shows the performance penalty compared to BPSK, QPSK, or dual polarization QPSK for high SNR [42].

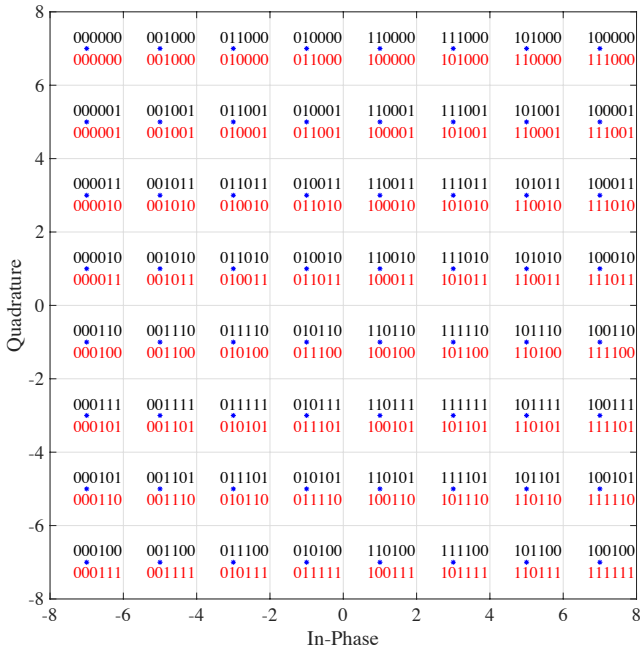

Figure 3.1: The natural and Gray labelings for 64-QAM constellations. The top black color indicates the Gray labeling and the bottom red color shows the natural binary labeling.

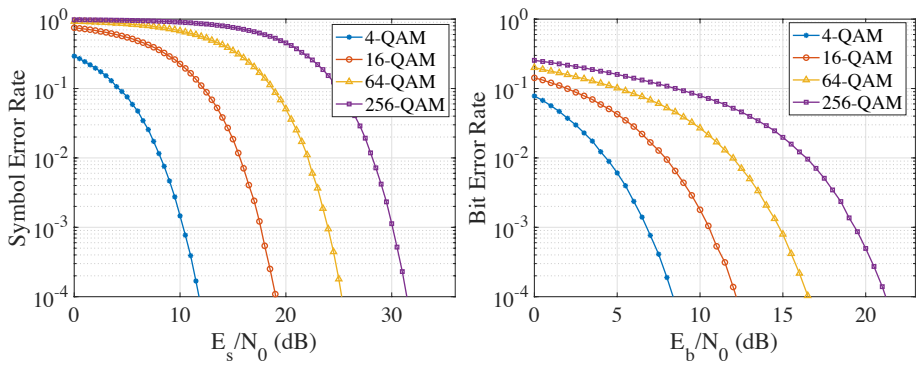

(a) SER **(b)** BER

Figure 3.2: The SER and uncoded BER performance of QAM formats with a uniform probability distribution over the AWGN channel. The BER is for Gray-mapped constellations.

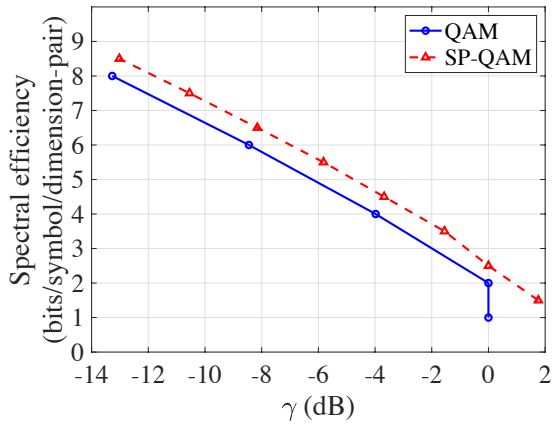

Figure 3.3: The SE vs APE (γ) for QAM and SP-QAM formats.

As an example, in Fig. 3.3, the relation between the SE and APE is shown for two groups of modulation formats, i.e., QAM and 4D set-partitioning (SP)-QAM [88, 89]. The SP-QAM is generated from the 4D QAM, which is a subset of $\mathbb{Z}^4$ lattice with a hypercube boundary, by removing every second point. Another way of constructing SP-QAM is by extension using integer lattice in $\{\mathbb{Z}^4 \cup (\mathbb{Z}^4 + \frac{\mathbf{1}}{\mathbf{2}})\}$, which is equivalent to D_4 lattice. Therefore, SP-QAM is a subset of D_4 lattice with a hybercube boundary. The analytical expression for SE and APE for QAM and SP-QAM are [90]

$$\text{QAM}: \quad \gamma = \frac{3SE}{2(2^{SE}-1)}, \quad SE/2 \text{ is integer} \tag{3.8}$$

$$\text{SP-QAM}: \quad \gamma = \begin{cases} \frac{3SE}{2^{(SE+0.5)}-1}, & SE+0.5 \text{ is even} \\ \frac{3SE}{2^{(SE+0.5)}-0.5}, & SE+0.5 \text{ is odd} \end{cases} \tag{3.9}$$

3.2.4 Mutual information

Since around 2010, soft-decision forward error correction (SD-FEC) schemes have become popular in the optical communication society because of their improved performance [91]. This improvement comes at the expense of higher complexity than hard-decision forward error correction (HD-FEC). In contrast to the HD-FEC decoder, which works with the

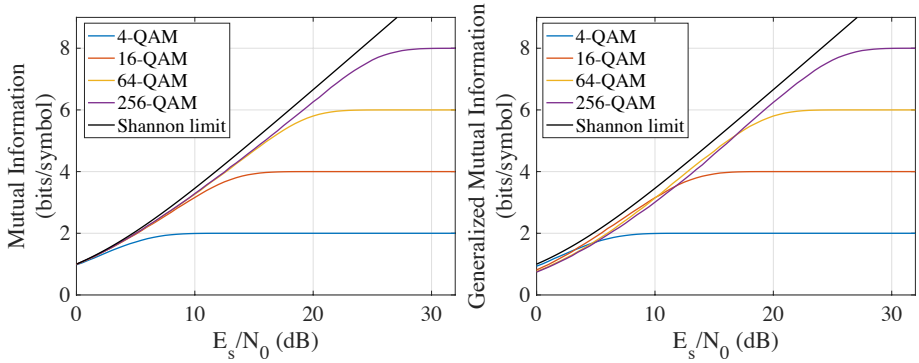

(a) MI **(b)** GMI

Figure 3.4: The MI and GMI performance of QAM formats over the AWGN channel. The Shannon limit is defined as $\log_2(1 + E_s/N_0)$.

estimated symbols or bits, the SD-FEC decoder depends on the soft information such as the likelihood of the received information. Therefore, for the SD-FEC decoder, there is not a direct relation between pre-forward error correction (FEC) and post-FEC BERs [92, 93]. A better metric for SD-FEC is the mutual information.

Assuming a discrete memoryless channel with multidimensional input vector $\mathbf{X}$, output vector $\mathbf{Y}$ in $\mathbb{R}^N$, and channel transition probability density function of $f_{\mathbf{Y}|\mathbf{X}}$, the mutual information (MI) is calculated as

$$\begin{aligned} MI = \mathbb{I}(\mathbf{X};\mathbf{Y}) &= \mathbb{E}\left[\log_2 \frac{f_{\mathbf{Y}|\mathbf{X}}(\mathbf{Y}|\mathbf{X})}{f_{\mathbf{Y}}(\mathbf{Y})}\right] = \mathbb{E}\left[\log_2 \frac{f_{\mathbf{X},\mathbf{Y}}(\mathbf{X},\mathbf{Y})}{f_{\mathbf{X}}(\mathbf{X}) f_{\mathbf{Y}}(\mathbf{Y})}\right] \\ &= \int_{\mathbb{R}^N}\int_{\mathbb{R}^N} f_{\mathbf{X},\mathbf{Y}}(\mathbf{x},\mathbf{y}) \log_2 \frac{f_{\mathbf{X},\mathbf{Y}}(\mathbf{x},\mathbf{y})}{f_{\mathbf{X}}(\mathbf{x}) f_{\mathbf{Y}}(\mathbf{y})} d\mathbf{x} d\mathbf{y} \\ &= \int_{\mathbb{R}^N}\int_{\mathbb{R}^N} f_{\mathbf{X}}(\mathbf{x}) f_{\mathbf{Y}|\mathbf{X}}(\mathbf{y}|\mathbf{x}) \log_2 \frac{f_{\mathbf{Y}|\mathbf{X}}(\mathbf{y}|\mathbf{x})}{f_{\mathbf{Y}}(\mathbf{y})} d\mathbf{x} d\mathbf{y} \\ &= \sum_{\mathbf{x}\in\mathcal{C}} P(\mathbf{x}) \int_{\mathbb{R}^N} f_{\mathbf{Y}|\mathbf{X}}(\mathbf{y}|\mathbf{x}) \log_2 \frac{f_{\mathbf{Y}|\mathbf{X}}(\mathbf{y}|\mathbf{x})}{f_{\mathbf{Y}}(\mathbf{y})} d\mathbf{y}, \end{aligned} \tag{3.10}$$

where the $f_{\mathbf{X}}$ and $f_{\mathbf{Y}}$ are the marginal distributions of the input and output and $f_{\mathbf{X},\mathbf{Y}}$ is the joint distribution. Since the input constellation points are discrete, the continuous integral over the input can be replaced with a discrete summation in the last step.

Instead of calculating the multidimensional integrals in (3.10), one

can use the Monte-Carlo method to approximate the MI as

$$MI \approx \frac{1}{K}\sum_{i=1}^{K}\log_2\frac{f_{\mathbf{Y}|\mathbf{X}}(\mathbf{y}_i|\mathbf{x}_i)}{f_{\mathbf{Y}}(\mathbf{y}_i)}, \tag{3.11}$$

where $(\mathbf{x}_i, \mathbf{y}_i)$ are K independent realization pairs, and $\mathbf{x}_i$ is drawn from $\mathcal{C}$ and transmitted through the simulated memoryless channel $f_{\mathbf{Y}|\mathbf{X}}$ to generate $\mathbf{y}_i$.

For a channel with input $\mathbf{X}$, symbol label of $b_0 b_1 \cdots b_{m-1}$, and output $\mathbf{Y}$, the mutual information can be expanded as

$$\begin{aligned}\mathbb{I}(\mathbf{X};\mathbf{Y}) &= \mathbb{I}(b_0, b_1, \cdots, b_{m-1};\mathbf{Y}) \\ &= \mathbb{I}(b_0;\mathbf{Y}) + \mathbb{I}(b_1;\mathbf{Y}|b_0) + \cdots + \mathbb{I}(b_{m-1};\mathbf{Y}|b_0, b_1, \cdots, b_{m-2}).\end{aligned} \tag{3.12}$$

In this equation, each term provides a binary-input channel and a binary code can be applied for error correction. This is referred as a multi-stage decoder where lower-index bit levels provide side information for decoding of higher level bits [94]. However, this scheme comes at the expense of latency, memory to store channel output, and an individual code for each sub-channel.

Similar to the BER, the generalized mutual information (GMI) depends on the bit labeling of the constellation points. The GMI is defined as an achievable information rate for a bit-wise decoder. Bit-wise decoder splits the decoding process into two stages, where first, soft information on the bits (logarithmic likelihood ratios) is calculated in a demapper, and then, one or multiple binary soft-decision (SD) decoder is used [95]. If we neglect the side conditioning in (3.12), the result will be known as the GMI

$$GMI = \mathbb{I}(b_0;\mathbf{Y}) + \mathbb{I}(b_1;\mathbf{Y}) + \cdots + \mathbb{I}(b_{m-1};\mathbf{Y}) = \sum_{i=0}^{m-1}\mathbb{I}(b_i;\mathbf{Y}). \tag{3.13}$$

A more general definition for GMI is given by equation (12) in [93]. In [Paper D], we use the GMI performance metric to study the best QAM formats in fiber links based on phase-insensitive or phase-sensitive amplifiers.

Generally, the MI is always greater than the GMI and the rate loss is due to the suboptimal bit-wise decoder. For Gray-labeling, this rate reduction has been shown to be very small [96]. The MI and GMI for QAM formats are shown in Fig. 3.4 over the AWGN channel.

Normalizing the GMI with the number of transmitted bits per symbol results in the normalized generalized mutual information (NGMI), i.e.,

$$NGMI = \frac{1}{m} GMI = \frac{1}{m} \sum_{i=0}^{m-1} \mathbb{I}(b_i; \mathbf{Y}). \tag{3.14}$$

For a nonuniform source, the NGMI is defined as [97, 98]

$$NGMI = 1 - \frac{\mathbb{H}(\mathbf{X}) - GMI}{\log_2 M}. \tag{3.15}$$

The NGMI can be used to predict the post-FEC BER in SD systems without implementing the encoder and decoder. Such predictions have been shown in [92] for different coding schemes and code rates. In [Paper C], we use NGMI to compare multidimensional modulation formats with QAM at different SEs.

CHAPTER 4

Constellation Shaping

The recent increasing demands for higher data rates in communication systems have forced the system designers to operate closer to channel capacity than before [99]. To achieve this goal, the source is optimized to maximize the mutual information between the input and output of the channel [100]. In information theory, this optimization is called *constellation shaping* and it is defined as finding energy-efficient methods for the communication system to improve the performance compared with the conventional QAM formats [101]. The horizontal gaps in the MI and GMI plots shown in Fig. 3.4 are the shaping gains that can be achieved compared with QAM formats.

In a simple approximation of the fiber-optic communication link showed in chapter 2, the optical fiber channel is assumed as an AWGN channel where the main source of noise is the amplified spontaneous emission noise from the optical amplifiers in the link. It has been shown that for an AWGN channel, under an average power constraint, the capacity achieving source distribution is the continuous Gaussian probability density function [102]. Therefore, the constellation distribution used in real systems should approximate the Gaussian distribution for the transmitted symbols.

Two main classifications of constellation shaping methods are PS and GS [98]. PS uses a nonuniform distribution over a regular, low-dimensional constellation such as QAM, whereas GS refers to a nonrect-

angular constellation, often multidimensional, with a uniform distribution [Paper B]. PS tries to achieve the AWGN channel capacity under an average power constraint by approximating a discrete Gaussian distribution for the input constellation. On the other hand, GS tries to rearrange the constellation points inside an approximately N-dimensional hypersphere boundary rather than a hypercube boundary to increase the energy efficiency as described in [103].

4.1 Probabilistic Shaping

The capacity of a communication channel under an average power constraint P is achieved by optimizing the mutual information over all distributions on the input that satisfy the power constraint [104], i.e.,

$$C = \max_{f_{\mathbf{X}}:\mathbb{E}\left[\|\mathbf{X}\|^2\right]\leq P} \mathbb{I}(\mathbf{X};\mathbf{Y}), \tag{4.1}$$

where C is the channel capacity with the optimum $f_{\mathbf{X}}$ and $\mathbb{I}$ denotes the mutual information. However, finding the optimum distribution is not always possible and sometimes the channel itself is mathematically complicated, e.g., the nonlinear optical fiber channel [25].

The PS is a method to employ source distributions other than the uniform distribution to increase the transmission information rate [30]. In an AWGN channel, the continuous Gaussian distribution maximizes the mutual information between the input and output of the channel under the constraint of limited input average power and results in the famous Shannon capacity formula [23]. However, continuous input distributions are not practical in real communication systems since the information unit, i.e., bits, are discrete and transmitting them over a channel requires discrete alphabets from a fixed set $\mathcal{C}$. Under the conditions of discrete and fixed input source alphabets with an maximum average power P, a discrete (or sampled) Gaussian distribution optimizes the MI in the AWGN channel [105].

Let the positive scalar ρ denote a constellation scaling of a fixed constellation $\mathcal{C}$. Furthermore, the probability of generating each symbol $\mathbf{x}$ in $\mathcal{C}$ is given by [30]

$$P(\mathbf{x}) = \frac{1}{\sum_{\mathbf{x}'\in\mathcal{C}} \exp(-\nu \left\|\mathbf{x}'\right\|^2)} \exp(-\nu \left\|\mathbf{x}\right\|^2), \tag{4.2}$$

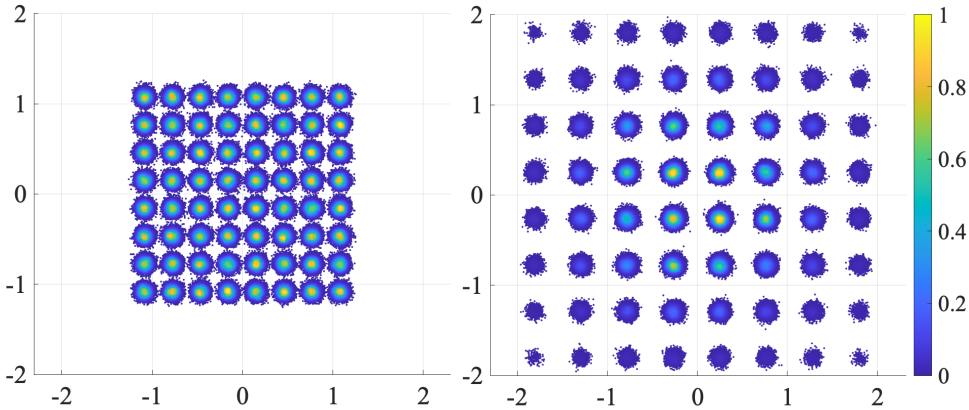

(a) $\nu = 0$ **(b)** $\nu = 2.69$

Figure 4.1: Uniform and probabilistically shaped 64-QAM at the same SNR with 6 and 5 bits/symbol source entropy, respectively. The color bar shows the normalized probability of occurrence.

where ν is the positive shaping factor [106] to control the source entropy and energy. For $\nu = 0$, the probability distribution becomes uniform and for $\nu > 0$, the constellation points will have a nonuniform probability. Increasing ν causes the inner points of the constellation to have higher probability than the outer constellation points as shown in Fig. 4.1. For each choice of ν, there exists a scaling ρ that fulfills the average-power constraint with equality. The MI between the input and output of the channel depends on the shaping factor ν, the scaling factor ρ, and the SNR. In fact, it has been shown that for every SNR, there is an optimum ν and ρ which maximizes the MI over the AWGN channel [107].

Choosing the optimized shaping factor at each SNR will change the source entropy at the corresponding SNR. On the other hand, setting the shaping factor to a fixed value for all SNRs will result in a source with a fixed source entropy. The effect of applying a constant shaping factor or optimizing the shaping factor at each SNR is shown in Fig. 4.2.

Different schemes have been suggested for the implementation of PS, and the one which has got most attention in the optical communications community is the probabilistic amplitude shaping (PAS). The PAS applies coding and shaping in an independent structure with separate optimizations, which reduces the problem of burst errors and shaping distortion compared with other realizations of PS [98]. In Fig. 4.3, the block diagram of a common realization of a PAS transmitter and receiver is pre-

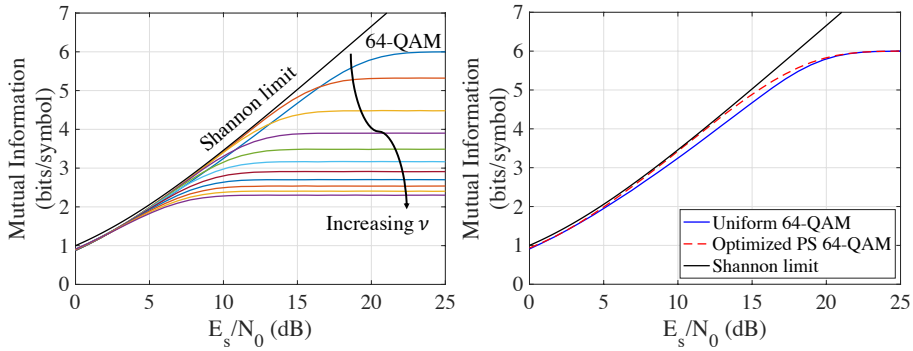

(a) Fixed ν for each curve.

(b) Optimized ν at each SNR.

Figure 4.2: Effect of changing the shaping factor ν on the MI of the transmitted and received symbols. The setup includes a discrete-time memoryless AWGN channel and linearly scaled QAM input with distribution in (4.2).

sented [108]. In the transmitter, the splitter divides the input bit stream into two branches. The top branch is fed into the distribution matcher which generates a group of amplitudes based on the desired probability distribution, e.g., the Gaussian distribution. This amplitudes are labeled in the Gray mapping block and generate another stream of bits. Together with the bottom branch, these bits are encoded by a systematic FEC encoder. After FEC encoding, the number of bits should be equal to the number of amplitudes after the distribution matcher. After the FEC encoder, the bits $\{b_i\}$ are used to form the sign bits using $(-1)^{b_i}$ mapping and generate one dimension of the constellation. With the same procedure in the other dimension, the probabilistically shaped QAM can be generated. In the receiver, the received dimension is decoded to generated the desired reliability metric for bits, which is fed into to the FEC decoder. Then, the inverse of shaping is applied to recover an estimate of the transmitted bits.

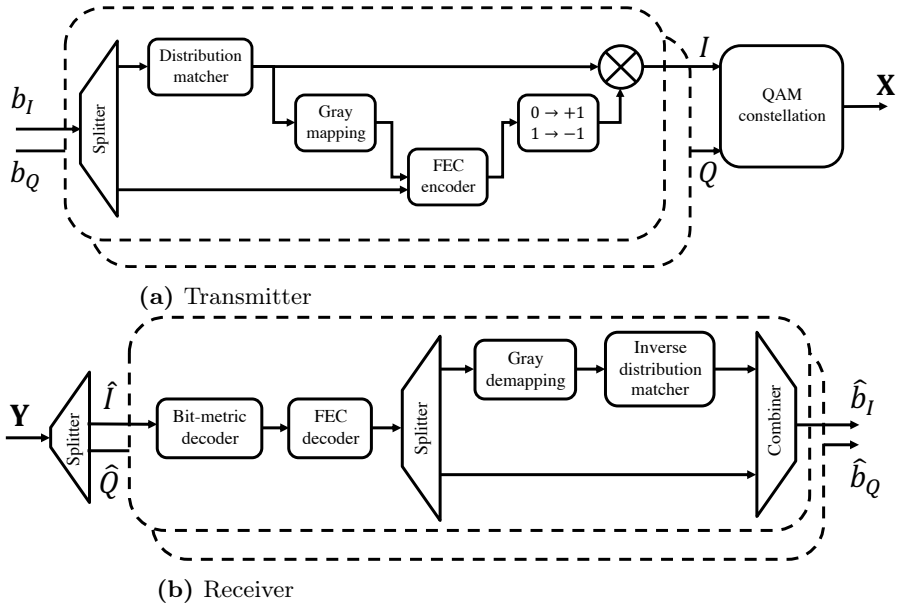

Figure 4.3: The transmitter and receiver block diagram for the PAS scheme with independent IQ components [108].

4.2 Geometric Shaping

Similar to PS, GS is also used to mimic the Gaussian distribution by another approach. Rather than changing the probability of generating each constellation point, for GS the probability of the constellation points is uniform; however, to shape the constellation, the position of constellation points in the Euclidean space is changed compared with the conventional cubic structures (QAM formats), which are widely used in communication systems. It has been shown that a high-dimensional, approximately spherical constellation with uniform distribution has a one-dimensional projection that is approximately Gaussian [103] .

Recently, GS has been investigated by optimizing the position of the constellation points in an irregular structure in two-dimensional space to optimize a metric such as GMI [109]. This approach becomes complicated as the number of constellation points or dimensionality increases, and because of the irregular and spherically distributed points, a look-up table is usually required to store the coordinates of the symbols.

Another method, which is in focus for this thesis, is multidimensional geometric shaping [103]. In this approach, instead of looking into irregu-

lar structures in Euclidean space, we use multidimensional lattice structures, which provide regular points set in the multidimensional space [86]. Lattices in multidimensional space can provide both shaping and coding gain with respect to cubic constellations with cubic boundaries. The shaping gain is achieved by a boundary which is closer to a hypersphere in the multidimensional space and coding gain comes from the denser packing of the points. The shaping gain shows the reduction in average energy required by a constellation bounded by $\mathcal{R}$ compared to that which would be required by a constellation bounded by an N-dimensional cube of the same volume. The coding gain is defined as the reciprocal of the number of constellation points per unit volume [44, Chap. 5].

Below, some of the known N-dimensional lattices are introduced.

- Cubic (integer) lattice
  This lattice is the famous structure from which the conventional QAM format is extracted with a hyper-cubic boundary. Generally, it is described as

$$\mathbb{Z}^N = \left\{ (x_0, x_1, \cdots, x_{N-1})^T \mid x_i \in \mathbb{Z} \right\}, \tag{4.3}$$

  where $\mathbb{Z}$ is the set of integer numbers, and ^{T} is the transpose operation.

- Hexagonal lattice
  This lattice is famous in 2 and 3 dimensions since it provides the optimum lattice packing in these dimensions. It can be described by

$$A_N = \left\{ (x_0, x_1, \cdots, x_N)^T \mid x_i \in \mathbb{Z}, \sum_i x_i = 0 \right\}. \tag{4.4}$$

- Checkerboard lattice
  A chess board can be considered as an example for this lattice in 2 dimensions. This lattice is described as

$$D_N = \left\{ (x_0, x_1, \cdots, x_{N-1})^T \mid x_i \in \mathbb{Z}, \sum_i x_i \equiv 0 \pmod 2 \right\}. \tag{4.5}$$

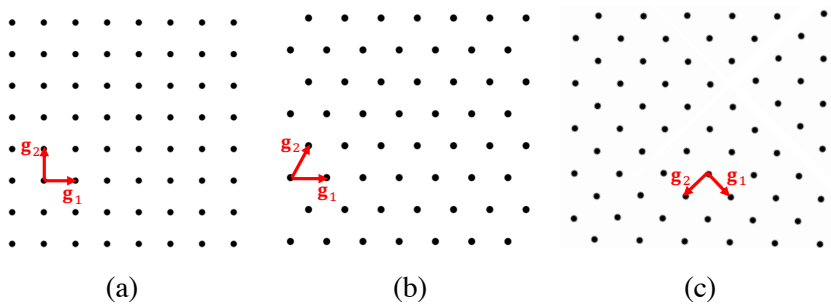

Figure 4.4: Example of lattices in 2 dimensions, (a) cubic, (b) hexagonal, and (c) checkerboard lattice. The basis vectors are shown in red arrows.

- Gosset lattice
  This lattice is defined in 8-dimensional space and it is described as [110]

$$E_8 = \left\{ \mathbf{x} = (x_0, x_1, \cdots, x_7)^T \mid \mathbf{x} \in D_8 \bigcup (D_8 + \frac{\mathbf{1}}{\mathbf{2}}) \right\}. \tag{4.6}$$

- Barnes–Wall lattice
  The Barnes–Wall lattice is a d-dimensional lattice that exists when d is a power of 2. In this work, it is defined in 16-dimensional space and can be constructed based on the first-order Reed–Muller code of length 16 [86, Chap. 4].

- Leech lattice
  This lattice is defined in 24-dimensional space and it provides the densest lattice packing in 24 dimensions [111]. There are many descriptions for this lattice [86, Chap. 24].

Examples of the first three lattices in 2 dimensions are shown in Fig. 4.4. Beside these descriptions, the points in a lattice can be easily generated using its *generator matrix* $\mathbf{G}$. The generator matrix consists of linearly independent column vectors called basis vectors $[\mathbf{g}_0, \mathbf{g}_1, \cdots, \mathbf{g}_{N-1}]$. Therefore, a lattice can be generated by

$$\Lambda = \{ z_0\mathbf{g}_0 + z_1\mathbf{g}_1 + \cdots + z_{N-1}\mathbf{g}_{N-1} \mid z_i \in \mathbb{Z} \} = \left\{ \mathbf{Gz} \mid \mathbf{z} \in \mathbb{Z}^N \right\}. \tag{4.7}$$

As defined in (4.7), lattices are infinite sets of points. In order to use them as a modulation format, a finite number of points inside a specific

Table 4.1: Shaping and coding gains of multidimensional lattices [112, Tab. I], [44, Tab. 5.3]

Lattice	$\mathbb{Z}^N$	A_2	D_4	E_8	BW_{16}	Λ_{24}
γ_c (dB)	0	0.62	1.51	3.01	4.52	6.02
γ_s (dB)	0	0.17	0.37	0.65	0.86	1.03

boundary should be selected. For instance, QAM formats are the points selected from $\mathbb{Z}^2$ within a square boundary. Other types of boundaries rather than the cubic boundary are circular boundary and the scaled Voronoi region. Constellation mapping and demapping using circular boundaries are difficult and usually require look-up tables to store the constellation points. Due to complexity and gain factors, the focus of our work has been on the scaled Voronoi region. The Voronoi region of a lattice is defined as the set of all points in $\mathbb{R}^N$ which are closer to the all-zero vector than any other lattice points. This region is closer to a hypersphere boundary compared to a hypercube boundary, and therefore it can provide shaping gain.

The APE of a constellation is related to both shaping and coding gains which are separable at high SEs. For lattices, these gains are [44, Chap. 5]

$$\gamma_s(\mathcal{R}) = \frac{1}{12} \frac{N \cdot V(\mathcal{R})^{1+2/N}}{\int_{\mathcal{R}} \|\mathbf{r}\|^2 \, d\mathbf{r}} \tag{4.8}$$

$$\gamma_c(\Lambda) = \frac{d_{min}^2}{V(\Lambda)^{2/N}}, \tag{4.9}$$

where $V(\mathcal{R})$ stands for the volume of the shaping region $\mathcal{R}$, and $V(\Lambda)$ is the fundamental lattice volume, which is equal to the Voronoi region of any lattice points. The shaping and coding gain of various lattices are given in Table 4.1

The encoding of bits to the constellation points inside the scaled Voronoi region and decoding from them have been discussed in detail in [Paper B].

CHAPTER 5

Physical Realization of Multidimensional Formats

In order to transmit information using multidimensional constellations in an optical communication system, information bits should be mapped to the physical dimensions of an optical signal. Intrinsically, an optical signal in a single-mode fiber has 4 physical dimensions at each wavelength and time slot, i.e., two orthogonal polarizations with IQ components in each of them. Multi-mode/multi-core fibers provide an extra degree of freedom in modes/cores to realize multidimensional formats. In this chapter, we investigate the possible practical realization of multidimensional modulation formats over the multidimensional space of optical signals.

5.1 Available physical dimensions

In optical communication links, the optical field at the output of the transmitter into the fiber channel can be modeled as

$$\mathbf{E}(t) = \sum_{p} \sum_{q} \sqrt{P_{p,q}(t)} e^{j(\frac{2\pi c_0}{n\lambda_{p,q}} t + \phi_{p,q}(t))} \mathbf{s}_{p,q}(t), \tag{5.1}$$

where $\mathbf{s}$ is the normalized complex envelope with a time-dependent amplitude and phase over the two orthogonal polarization states. The P, λ, and ϕ indicate the power, wavelength, phase of the optical carrier. Indices p and q show the number of different wavelength channels that

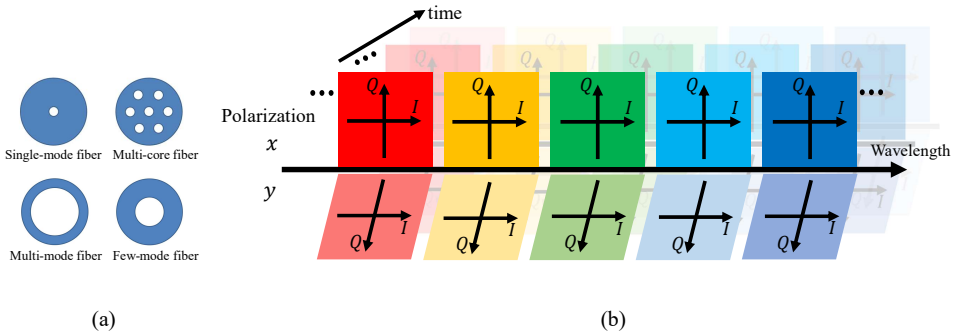

Figure 5.1: (a) Examples of fibers to realize the spatial dimension (b) Available physical dimensions in one mode/core of a fiber. Different colors indicate different wavelengths. At each wavelength, two orthogonal polarizations and IQ components can be used.

are propagating together and the number of cores/modes in the fiber, respectively, as shown in fig. 5.1. The c_0 and n are the speed of light in vacuum and the refractive index of the fiber, respectively.

In each core and wavelength, the complex envelope is described by a complex vector

$$\mathbf{s}(t) = \sum_k \mathbf{c}_k \cdot h(t - kT), \quad \mathbf{c}_k = \begin{bmatrix} I_x^k + jQ_x^k \\ I_y^k + jQ_y^k \end{bmatrix}, \tag{5.2}$$

where I and Q are real numbers indicating the IQ components of the electrical field, respectively. The x and y stand for the two orthogonal polarization states. Also, k indicates the time slot in which the data is transmitted and $h(t)$ is the pulse shaping function with duration T and unit average energy.

In Eq. (5.1) and (5.2), the degrees of freedom which can be used to modulate an optical signal in a multi-core fiber are IQ components, polarizations, time slots, wavelengths, and cores/modes. In each core, wavelength, and polarization component, the corresponding complex envelope can be geometrically represented in the Cartesian coordinate system, where one axis is used to present the real part of the complex number (I) and the other axis shows the imaginary part (Q).

Alternatively, the combinations of all available IQ components, polarizations, wavelengths, spatial modes, and time slots can be considered orthogonal dimensions. In this approach, the transmitted signal is rep-

resented as

$$\mathbf{E}(t) = \sum_{k} \sum_{d=0}^{N-1} c_{k,d} \Phi_d(t - kT_{ts}), \tag{5.3}$$

where the real vector $\mathbf{c}_k = [c_{k,0}, c_{k,1}, \cdots, c_{k,N-1}]$ is the kth transmitted symbol, N is the dimensionality, T_{ts} is total duration of the occupied time slots to realize each multidimensional symbol, and $\{\Phi_d(t)\}$ is the set of all possible combinations of dimensions including IQ components, polarization, wavelengths, spatial modes, and time slots. The combination of these dimensions generates a set whose elements are orthogonal to each other, not only in time but also in frequency, polarization, space, and quadrature components, i.e.,

$$\frac{1}{T} \int_0^T \Phi_d(t) \Phi_{d'}^*(t) dt = \delta_{d,d'}, \tag{5.4}$$

where δ is the Kronecker delta function, and * is the conjugate operation.

5.2 2D projection

Grouping the N-dimensional constellation into pair of dimensions (2D projection) can be done in different combinations. For example, in Fig. 5.2, we present two grouping of dimensions resulting in different 2D projections by combing pairs of real dimensions together. These realizations can generate different number of levels or different probability distribution for each group which can affect the performance of the physical realization.

After the 2D projection, each 2D group can be realized over a time slot in each polarization, wavelength, and spatial mode. These physical realizations can provide different performances depending on the DSP algorithm that is used in the receiver to compensate the channel and transceiver impairments. A detailed discussion about the comparison of different physical realization is presented in [Paper C].

5.3 Physical realization

In an experimental setup, multidimensional formats are implemented by DACs and MZMs. One possible realization of these formats is shown in Fig. 5.3 over a single-mode fiber channel. In this case, IQ components

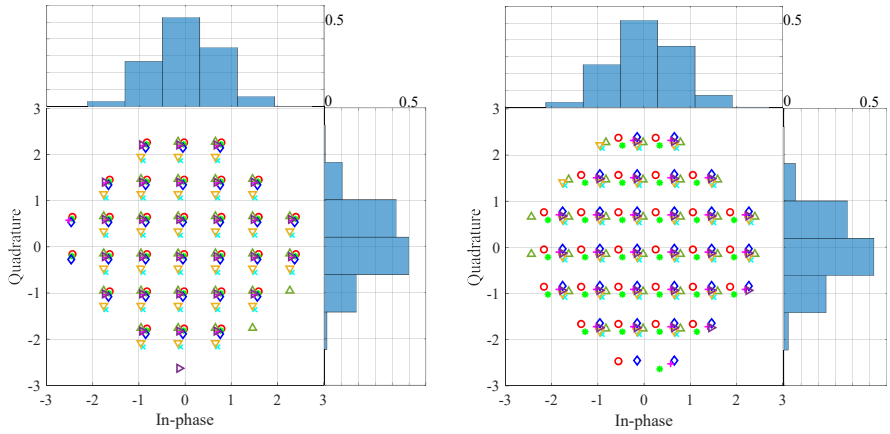

Figure 5.2: (a) and (b) Two random 2D projections of a 16D modulation format based on the Barnes–Wales lattice. The bars on the top and the right side of the constellations shows the overall normalized histogram of the symbols in the constellation.

and polarizations create a 4D space and the rest of the constellation dimensions are implemented over time slots. The main impairments over the fiber channel are the polarization mixing, dispersion, attenuation, and self-phase modulation (SPM) due to Kerr effect.

In another realization shown in Fig. 5.4, constellation dimensions are mapped to different wavelengths in a WDM system. In this scenario, multiple wavelengths can be used to reduce the usage of consecutive time slots and therefore reducing the delay time to send a multidimensional symbol. On the other hand, this scheme comes with increased hardware complexity and synchronization between different wavelengths compared ot Fig. 5.3. In addition to the channel impairments in the single wavelength realization case, cross-phase modulation (XPM) and four-wave mixing (FWM) can affect the performance of the system.

Another possible method for future systems will be space-division multiplexing (SDM), shown in Fig. 5.5, where the spatial dimension together with WDM systems are deployed together. In this case, cross-talk between the modes or cores can degrade the performance.

Figure 5.3: Single carrier transmission over a single-mode fiber. In this case, the multidimensional constellations are realized over two polarizations, IQ components, and multiple time slots in a single carrier.

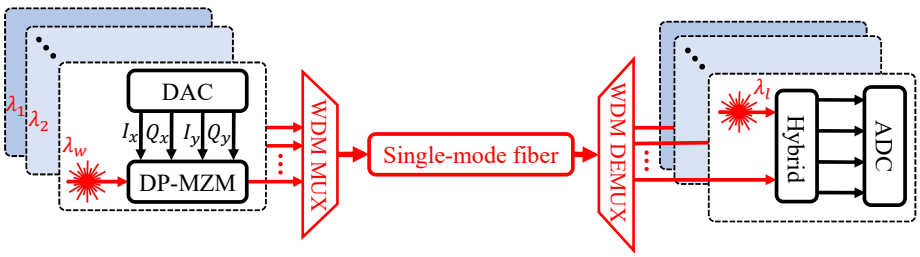

Figure 5.4: Multi-wavelength transmission over a single-mode fiber. Constellation dimensions are divided into 4D groups, each one realized over an optical carrier. Consecutive time slots can be used if $N/4$ is greater than the number of wavelengths.

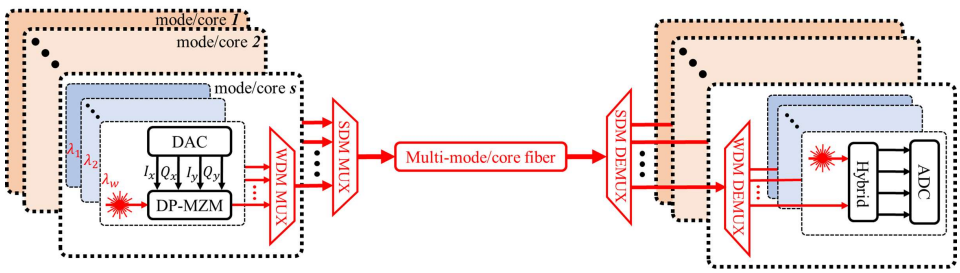

Figure 5.5: Multi-wavelength transmission over a multi-mode/core fiber. Spatial dimensions together with wavelengths, polarization, time slots, and IQ components are used to carry multidimensional symbols.

CHAPTER 6

Future outlook

In this chapter, some future related topics to this thesis are discussed.

Multidimensional geometric shaping can be further investigated in scenarios including:

Gausian-noise (GN) and enhanced-GN (EGN) models validation for Voronoi constellations
To reduce the simulation time of the SSFM in long-haul fiber transmission, validating the GN and EGN models for Voronoi constellation will not only speed-up the performance estimation of constellations but also give a better insight on the higher-order moments behavior of these constellations.

Performance with both the transmitter and channel impairments
In this thesis, only the optical fiber channel impairments has been considered for the geometrically shaped constellations. Because of the non-ideal components of the transmitter in real systems, e.g., DAC and MZM, geometrically shaped constellation could perform differently because of their peak-to-average power ratio.

The MI and GMI metrics
Because of high dimensionality and constellations sized for Voronoi constellations (VCs), the computation of MI and GMI is very time consuming. Exploring low-complexity methods to estimate these metrics is an interesting research topic for future works. Moreover, designing multilevel coding (MLC) schemes can help to improve the performance of VCs combined with SD-FEC compared to QAM formats.

Efficient bit labeling
The performance of lattice-based constellations has been investigated in terms of BER in this thesis and natural and quasi-Gray bit labeling have been used to label the symbols. Investigating a more efficient bit labeling for these constellations by applying machine learning techniques can be considered for more improvements.

Comparison with probabilistic shaping methods
A comprehensive comparison between multidimensional geometric shaping and probabilistic shaping can determine the advantages and disadvantages of each methods in different operation regimes. Implementation complexity of these methods is also an important aspect which can affect the power consumption of the optical systems.

CHAPTER 7

Summary of papers

Paper A
Lattice-based geometric shaping
European Conference on Optical Communication (ECOC), Brussels, Belgium, Dec 2020.

In this paper, lattice-based constellations have been investigated, but here in terms of SER without considering the bit labeling. The multi-dimensional constellations have been realized using frequency, polarizations, and IQ components. We demonstrate more than 78% transmission reach and 4.5 dB power improvements compared to uniform QAM formats at the same normalized symbol error rate.

Paper B
Low-complexity geometric shaping
Journal of Lightwave Technology, vol. 39, no. 2, pp. 363-371, Jan 2021.

In this paper, we have investigated the performance of multidimensional geometric shaping based on lattices. Fast and low-complexity algorithms have been used to make the transmission and detection of high-cardinality constellations possible. Simulations have been done over the linear AWGN and nonlinear fiber optic channels using the split-step Fourier method. Two low-complexity bit labeling approaches have been

studied to explore the uncoded BER. Over the nonlinear fiber channel, we demonstrate more than 38% reach improvements compared to 4-QAM.

Paper C
Physical realizations of multidimensional Voronoi constellations in optical communication systems
submitted to *Journal of Lightwave Technology*, Nov 2022.

In this paper, physical realizations of multidimensional VCs are investigated both in simulations and experiments, and compared over the nonlinear fiber channel. Constellations up to 32 dimensions and spectral efficiencies of 4 bits/symb/dimension-pair are demonstrated. We show approximately similar performances between different physical realizations of VCs.

Paper D
Capacity of phase-sensitively preamplified optical links at low signal-to-noise ratio
European Conference on Optical Communication (ECOC), Basel, Switzerland, Sep 2022.

In this paper, we study fiber links based on phase-insensitive amplifiers and phase-sensitive amplifiers both in simulation and experiment. The best QAM formats in low signal-to-noise ratio in these links are identified and their performances are quantified.

Paper E
Comparison of uniform cross QAM and probabilistically shaped QAM formats under the impact of transmitter impairments
European Conference on Optical Communication (ECOC), Dublin, Ireland, Sep 2019.

In this paper, the impact of transmitter impairments including the DAC and MZM are explored for probabilistically shaped QAM and cross-QAM constellations. The fiber channel is considered as an AWGN channel. We demonstrate that cross-QAM outperforms PS-QAM by a factor of up to 4 in symbol error rate and higher achievable information rates, at the same source entropy and optimal electrical signal powers.

Paper F
Performance of probabilistic shaping coherent channels in hybrid systems
International Conference on Transparent Optical Networks (ICTON), Bari, Italy, July 2020.

In this paper, the performance of probabilistically shaped QAM formats is compared with uniform QAM in links where higher order modulation formats co-propagate with legacy OOK channels. The results show that increasing the number of OOK channels, increases the nonlinear effects on the coherent channels and the performance of uniform QAM formats degrade faster compared to probabilistically shaped QAM.

References

[1] A. Sun and X. Chen, "Online education and its effective practice: A research review." *Journal of Information Technology Education*, vol. 15, 2016.

[2] A. Feldmann, O. Gasser, F. Lichtblau, E. Pujol, I. Poese, C. Dietzel, D. Wagner, M. Wichtlhuber, J. Tapiador, N. Vallina-Rodriguez *et al.*, "The lockdown effect: Implications of the COVID-19 pandemic on internet traffic," in *Proceedings of the ACM Internet Measurement Conference*, 2020, pp. 1–18.

[3] M. Candela, V. Luconi, and A. Vecchio, "Impact of the COVID-19 pandemic on the internet latency: A large-scale study," *Computer Networks*, vol. 182, p. 107495, 2020.

[4] R. Hui, *Introduction to fiber-optic communications.* Academic Press, 2019.

[5] A. L. Schawlow and C. H. Townes, "Infrared and optical masers," *Physical Review*, vol. 112, no. 6, p. 1940, 1958.

[6] W. Koechner, *Solid-state laser engineering.* Springer, 2013, vol. 1.

[7] H. Murata, *Handbook of optical fibers and cables.* CRC Press, 2020, vol. 1.

[8] T. H. MAIMAN, "Stimulated optical radiation in ruby," *Nature*, vol. 187, no. 4736, pp. 493–494, Aug 1960. [Online]. Available: https://doi.org/10.1038/187493a0

[9] A. Javan, W. R. Bennett Jr, and D. R. Herriott, "Population inversion and continuous optical maser oscillation in a gas discharge containing a He-Ne mixture," *Physical Review Letters*, vol. 6, no. 3, p. 106, 1961.

[10] R. N. Hall, G. E. Fenner, J. Kingsley, T. Soltys, and R. Carlson, "Coherent light emission from GaAs junctions," *Physical Review Letters*, vol. 9, no. 9, p. 366, 1962.

[11] B. I. Hirschowitz, "Photography through the fiber gastroscope," *The American journal of digestive diseases*, vol. 8, no. 5, pp. 389–395, 1963.

[12] F. Kapron, D. B. Keck, and R. D. Maurer, "Radiation losses in glass optical waveguides," *Applied Physics Letters*, vol. 17, no. 10, pp. 423–425, 1970.

[13] R. Csencsits, P. Lemaire, W. Reed, D. Shenk, and K. Walker, "Fabrication of low-loss single-mode fibers," in *Optical Fiber Communication Conference (OFC)*, 1984, p. TuI3.

[14] H. Yokota, H. Kanamori, Y. Ishiguro, G. Tanaka, S. Tanaka, H. Takada, M. Watanabe, S. Suzuki, K. Yano, M. Hoshikawa *et al.*, "Ultra-low-loss pure-silica-core single-mode fiber and transmission experiment," in *Optical Fiber Communication Conference (OFC)*, 1986, p. PD3.

[15] R. Kerdock and D. Wolaver, "Atlanta fiber system experiment: results of the atlanta experiment," *Bell System Technical Journal*, vol. 57, no. 6, pp. 1857–1879, 1978.

[16] I. Jacobs, "Atlanta fiber system experiment: Overview," *Bell System Technical Journal*, vol. 57, no. 6, pp. 1717–1721, 1978.

[17] R. J. Mears, L. Reekie, I. Jauncey, and D. N. Payne, "Low-noise erbium-doped fibre amplifier operating at 1.54 μm," *Electronics Letters*, vol. 23, no. 19, pp. 1026–1028, 1987.

[18] J. M. Simmons, *Optical network design and planning.* Springer, 2014.

[19] C.-H. Yeh, C.-C. Lee, and S. Chi, "120-nm bandwidth erbium-doped fiber amplifier in parallel configuration," *IEEE Photonics Technology Letters*, vol. 16, no. 7, pp. 1637–1639, 2004.

[20] G. P. Agrawal, "Optical communication: its history and recent progress," in *Optics in our time*. Springer, Cham, 2016.

[21] S. Tsukamoto, D.-S. Ly-Gagnon, K. Katoh, and K. Kikuchi, "Coherent demodulation of 40-Gbit/s polarization-multiplexed QPSK signals with 16-GHz spacing after 200-km transmission," in *Optical Fiber Communication Conference (OFC)*, 2005, p. PDP29.

[22] P. J. Winzer and R.-J. Essiambre, "Advanced optical modulation formats," *Optical Fiber Telecommunications VB*, pp. 23–93, 2008.

[23] C. E. Shannon, "A mathematical theory of communication," *Bell system technical journal*, vol. 27, no. 3 and 4, pp. 379–423 and 623–656, 1948.

[24] R.-J. Essiambre, G. Kramer, P. J. Winzer, G. J. Foschini, and B. Goebel, "Capacity limits of optical fiber networks," *Journal of Lightwave Technology*, vol. 28, no. 4, pp. 662–701, 2010.

[25] E. Agrell, A. Alvarado, G. Durisi, and M. Karlsson, "Capacity of a nonlinear optical channel with finite memory," *Journal of Lightwave Technology*, vol. 32, no. 16, pp. 2862–2876, 2014.

[26] E. Agrell, "Conditions for a monotonic channel capacity," *IEEE Transactions on Communications*, vol. 63, no. 3, pp. 738–748, 2014.

[27] ——, "Nonlinear fiber capacity," in *European Conference and Exhibition on Optical Communication (ECOC)*, 2013.

[28] H. Dzieciol, G. Liga, E. Sillekens, P. Bayvel, and D. Lavery, "Geometric shaping of 2-D constellations in the presence of laser phase noise," *Journal of Lightwave Technology*, vol. 39, no. 2, pp. 481–490, 2020.

[29] B. Chen, Y. Lei, D. Lavery, C. Okonkwo, and A. Alvarado, "Rate-adaptive coded modulation with geometrically-shaped constellations," in *2018 Asia Communications and Photonics Conference (ACP)*, 2018.

[30] T. Fehenberger, A. Alvarado, G. Böcherer, and N. Hanik, "On probabilistic shaping of quadrature amplitude modulation for the nonlinear fiber channel," *Journal of Lightwave Technology*, vol. 34, no. 21, pp. 5063–5073, 2016.

[31] T. Fehenberger, "Information rates of probabilistically shaped coded modulation for a multi-span fiber-optic communication system with 64QAM," *Optics Communications*, vol. 409, pp. 2–6, 2018.

[32] I. F. de Jauregui Ruiz, A. Ghazisaeidi, O. A. Sab, P. Plantady, A. Calsat, S. Dubost, L. Schmalen, V. Letellier, and J. Renaudier, "25.4-Tb/s transmission over transpacific distances using truncated probabilistically shaped PDM-64QAM," *Journal of Lightwave Technology*, vol. 36, no. 6, pp. 1354–1361, 2018.

[33] J.-X. Cai, H. Batshon, M. V. Mazurczyk, O. V. Sinkin, D. Wang, M. Paskov, W. Patterson, C. R. Davidson, P. Corbett, G. Wolter *et al.*, "70.4 Tb/s capacity over 7,600 km in C+L band using coded modulation with hybrid constellation shaping and nonlinearity compensation," in *Optical Fiber Communication Conference (OFC)*, 2017, pp. Th5B–2.

[34] J.-X. Cai, H. G. Batshon, M. V. Mazurczyk, O. V. Sinkin, D. Wang, M. Paskov, C. R. Davidson, W. W. Patterson, A. Turukhin, M. A. Bolshtyansky *et al.*, "51.5 Tb/s capacity over 17,107 km in C+L bandwidth using single-mode fibers and nonlinearity compensation," *Journal of Lightwave Technology*, vol. 36, no. 11, pp. 2135–2141, 2018.

[35] T. Kanada, Y. Okano, K. Aoyama, and T. Kitami, "Design and performance of WDM transmission systems at 6.3 Mbits/s," *IEEE transactions on communications*, vol. 31, no. 9, pp. 1095–1102, 1983.

[36] F. Buchali, V. Aref, M. Chagnon, K. Schuh, H. Hettrich, A. Bielik, L. Altenhain, M. Guntermann, R. Schmid, and M. Moller, "1.52 Tb/s single carrier transmission supported by a 128 GSa/s SiGe DAC," in *Optical Fiber Communication Conference (OFC)*, 2020, pp. Th4C–2.

[37] M. Mazur, J. Schröder, A. Lorences-Riesgo, T. Yoshida, M. Karlsson, and P. A. Andrekson, "11.5 bits/s/Hz PM-256QAM comb-based superchannel transmission by combining optical and digital pilots," in *Optical Fiber Communications Conference (OFC)*, 2018.

[38] S. J. Savory and D. S. Millar, "DSP for optical transponders," in *Springer Handbook of Optical Networks*. Springer, 2020, pp. 155–176.

[39] J. C. Rasmussen, T. Takahara, T. Tanaka, Y. Kai, M. Nishihara, T. Drenski, L. Li, W. Yan, and Z. Tao, "Digital signal processing for short reach optical links," in *European Conference on Optical Communication (ECOC)*, 2014.

[40] D. A. Huffman, "A method for the construction of minimum-redundancy codes," *Proceedings of the IRE*, vol. 40, no. 9, pp. 1098–1101, 1952.

[41] A. G. i Amat and L. Schmalen, "Forward error correction for optical transponders," in *Springer Handbook of Optical Networks*. Springer, 2020, pp. 177–257.

[42] E. Agrell and M. Karlsson, "Power-efficient modulation formats in coherent transmission systems," *Journal of Lightwave Technology*, vol. 27, no. 22, pp. 5115–5126, 2009.

[43] M. Karlsson and E. Agrell, "Four-dimensional optimized constellations for coherent optical transmission systems," in *European Conference on Optical Communication (ECOC)*, 2010.

[44] S. Benedetto and E. Biglieri, *Principles of Digital Transmission: with Wireless Applications*. Springer, 1999.

[45] J. Proakis, *Digital Communications*, ser. Communications and signal processing. McGraw-Hill, 1995.

[46] A. Gorlov, A. Gelgor, and V. P. Nguyen, "Root-raised cosine versus optimal finite pulses for faster-than-Nyquist generation," in *Internet of Things, Smart Spaces, and Next Generation Networks and Systems*. Springer, 2016, pp. 628–640.

[47] M. Joost, "Theory of root-raised cosine filter," *Research and Development*, vol. 47829, 2010.

[48] P. Gou, L. Zhao, K. Wang, W. Zhou, and J. Yu, "Nonlinear look-up table predistortion and chromatic dispersion precompensation for IM/DD PAM-4 transmission," *IEEE Photonics Journal*, vol. 9, no. 5, 2017.

[49] K. Roberts, C. Li, L. Strawczynski, M. O'Sullivan, and I. Hardcastle, "Electronic precompensation of optical nonlinearity," *IEEE Photonics Technology Letters*, vol. 18, no. 2, pp. 403–405, 2006.

[50] A. Napoli, P. W. Berenguer, T. Rahman, G. Khanna, M. M. Mezghanni, L. Gardian, E. Riccardi, A. C. Piat, S. Calabrò, S. Dris *et al.*, "Digital pre-compensation techniques enabling high-capacity bandwidth variable transponders," *Optics Communications*, vol. 409, pp. 52–65, 2018.

[51] C. Schmidt, C. Kottke, V. Jungnickel, and R. Freund, "High-speed digital-to-analog converter concepts," in *Next-Generation Optical Communication: Components, Sub-Systems, and Systems VI*, vol. 10130. International Society for Optics and Photonics, 2017, p. 101300N.

[52] C. Laperle and M. O'Sullivan, "Advances in high-speed DACs, ADCs, and DSP for optical coherent transceivers," *Journal of lightwave technology*, vol. 32, no. 4, pp. 629–643, 2014.

[53] D. Rafique, A. Napoli, S. Calabro, and B. Spinnler, "Digital preemphasis in optical communication systems: On the DAC requirements for terabit transmission applications," *Journal of Lightwave Technology*, vol. 32, no. 19, pp. 3247–3256, 2014.

[54] A. Napoli, M. M. Mezghanni, T. Rahman, D. Rafique, R. Palmer, B. Spinnler, S. Calabrò, C. Castro, M. Kuschnerov, and M. Bohn, "Digital compensation of bandwidth limitations for high-speed DACs and ADCs," *Journal of Lightwave Technology*, vol. 34, no. 13, pp. 3053–3064, 2016.

[55] K. Kikuchi, "Fundamentals of coherent optical fiber communications," *Journal of Lightwave Technology*, vol. 34, no. 1, pp. 157–179, 2015.

[56] A. Napoli, M. M. Mezghanni, D. Rafique, V. A. Sleiffer, B. Spinnler, and M. Bohn, "Novel digital pre-distortion techniques for low-extinction ratio Mach-Zehnder modulators," in *Optical Fiber Communication Conference (OFC)*, 2015, pp. Th3G–1.

[57] D. Rafique, H. Griesser, and J.-P. Elbers, "Enabling 64Gbaud coherent optical transceivers," in *Optical Fiber Communications Conference(OFC)*, 2017.

[58] A. F. Alfredsson, E. Agrell, and H. Wymeersch, "Iterative detection and phase-noise compensation for coded multichannel optical transmission," *IEEE Transactions on Communications*, vol. 67, no. 8, pp. 5532–5543, 2019.

[59] D. Villafani, A. Mirani, X. Pang, E. Goobar, J. Schröder, M. Karlsson, and P. Andrekson, "Phase noise characterization and EEPN of a full C-band tunable laser in coherent optical systems," *IEEE Photonics Technology Letters*, vol. 31, no. 24, pp. 1991–1994, 2019.

[60] K.-P. Ho, *Phase-modulated optical communication systems*. Springer Science & Business Media, 2005.

[61] Z. Jia, H.-C. Chien, J. Zhang, Z. Dong, and Y. Cai, "Performance analysis of pre-and post-compensation for bandwidth-constrained signal in high-spectral-efficiency optical coherent systems," in *Optical Fiber Communication Conference (OFC)*, 2014.

[62] I. Fatadin, S. J. Savory, and D. Ives, "Compensation of quadrature imbalance in an optical QPSK coherent receiver," *IEEE Photonics Technology Letters*, vol. 20, no. 20, pp. 1733–1735, 2008.

[63] A. B. Dar and R. K. Jha, "Chromatic dispersion compensation techniques and characterization of fiber Bragg grating for dispersion compensation," *Optical and Quantum Electronics*, vol. 49, no. 3, p. 108, 2017.

[64] S. J. Savory, G. Gavioli, R. I. Killey, and P. Bayvel, "Electronic compensation of chromatic dispersion using a digital coherent receiver," *Optics Express*, vol. 15, no. 5, pp. 2120–2126, 2007.

[65] F. Gardner, "A BPSK/QPSK timing-error detector for sampled receivers," *IEEE Transactions on Communications*, vol. 34, no. 5, pp. 423–429, 1986.

[66] S. J. Savory, "Digital coherent optical receivers: Algorithms and subsystems," *IEEE Journal of Selected Topics in Quantum Electronics*, vol. 16, no. 5, pp. 1164–1179, 2010.

[67] M. Mazur, J. Schröder, A. Lorences-Riesgo, T. Yoshida, M. Karlsson, and P. A. Andrekson, "Overhead-optimization of pilot-based digital signal processing for flexible high spectral efficiency transmission," *Optics Express*, vol. 27, no. 17, pp. 24 654–24 669, 2019.

[68] E. Ip and J. M. Kahn, "Compensation of dispersion and nonlinear impairments using digital backpropagation," *Journal of Lightwave Technology*, vol. 26, no. 20, pp. 3416–3425, 2008.

[69] T. Sasaki, T. Hasegawa, and H. Ishikawa, "Optical fiber and cables," *Springer Handbook of Optical Networks*, pp. 25–49, 2020.

[70] A. Larsson, P. Westbergh, J. Gustavsson, Å. Haglund, and B. Kögel, "High-speed VCSELs for short reach communication," *Semiconductor science and technology*, vol. 26, no. 1, p. 014017, 2010.

[71] G. P. Agrawal, *Nonlinear Fiber Optics*, 5th ed. Springer, 2013.

[72] T. A. Eriksson, T. Fehenberger, P. A. Andrekson, M. Karlsson, N. Hanik, and E. Agrell, "Impact of 4D channel distribution on the achievable rates in coherent optical communication experiments," *Journal of Lightwave Technology*, vol. 34, no. 9, pp. 2256–2266, 2016.

[73] S. Mumtaz, R.-J. Essiambre, and G. P. Agrawal, "Nonlinear propagation in multimode and multicore fibers: Generalization of the Manakov equations," *Journal of Lightwave Technology*, vol. 31, no. 3, pp. 398–406, 2012.

[74] C. Antonelli, M. Shtaif, and A. Mecozzi, "Modeling of nonlinear propagation in space-division multiplexed fiber-optic transmission," *Journal of Lightwave Technology*, vol. 34, no. 1, pp. 36–54, 2015.

[75] S. Li, M. Karlsson, and E. Agrell, "Improved simulation accuracy of the split-step Fourier method," in *Optical Fiber Communication Conference (OFC)*, 2020, pp. W2A–55.

[76] P. Poggiolini, "The GN model of non-linear propagation in uncompensated coherent optical systems," *Journal of Lightwave Technology*, vol. 30, no. 24, pp. 3857–3879, 2012.

[77] E. Agrell, G. Durisi, and P. Johannisson, "Information-theory-friendly models for fiber-optic channels: A primer," in *Information Theory Workshop (ITW)*, 2015.

[78] M. Sjödin, B. J. Puttnam, P. Johannisson, S. Shinada, N. Wada, P. A. Andrekson, and M. Karlsson, "Transmission of PM-QPSK and PS-QPSK with different fiber span lengths," *Optic Express*, vol. 20, no. 7, pp. 7544–7554, Mar 2012.

[79] E. Agrell, M. Karlsson, A. Chraplyvy, D. J. Richardson, P. M. Krummrich, P. Winzer, K. Roberts, J. K. Fischer, S. J. Savory, B. J. Eggleton *et al.*, "Roadmap of optical communications," *Journal of Optics*, vol. 18, no. 6, p. 063002, 2016.

[80] M. Karlsson and E. Agrell, "Multidimensional Modulation and Coding in Optical Transport," *Journal of Lightwave Technology*, vol. 35, no. 4, pp. 876–884, 2016.

[81] D. S. Millar, T. Koike-Akino, S. Ö. Arık, K. Kojima, K. Parsons, T. Yoshida, and T. Sugihara, "High-dimensional modulation for coherent optical communications systems," *Optics Express*, vol. 22, no. 7, pp. 8798–8812, 2014.

[82] T. A. Eriksson, P. Johannisson, E. Agrell, P. A. Andrekson, and M. Karlsson, "Biorthogonal modulation in 8 dimensions experimentally implemented as 2PPM-PS-QPSK," in *Optical Fiber Communication Conference (OFC)*, 2014.

[83] S. J. Savory, "Digital signal processing options in long haul transmission," in *Optical Fiber Communication Conference (OFC)*, 2008, p. OTuO3.

[84] Z. Qu, I. B. Djordjevic, and J. Anderson, "Two-dimensional constellation shaping in fiber-optic communications," *Applied sciences*, vol. 9, no. 9, p. 1889, 2019.

[85] D. Pilori, A. Nespola, F. Forghieri, and G. Bosco, "Non-linear phase noise mitigation over systems using constellation shaping," *Journal of Lightwave Technology*, vol. 37, no. 14, pp. 3475–3482, 2019.

[86] J. H. Conway and N. J. A. Sloane, *Sphere Packings, Lattices and Groups*, 3rd ed. Springer, 1999.

[87] M. Karlsson and E. Agrell, "Power-efficient modulation schemes," in *Impact of Nonlinearities on Fiber Optic Communications*. Springer, 2011, pp. 219–252.

[88] G. Ungerboeck, "Channel coding with multilevel/phase signals," *IEEE transactions on Information Theory*, vol. 28, no. 1, pp. 55–67, 1982.

[89] J. K. Fischer, C. Schmidt-Langhorst, S. Alreesh, R. Elschner, F. Frey, P. W. Berenguer, L. Molle, M. Nölle, and C. Schubert, "Generation, transmission, and detection of 4-D set-partitioning QAM signals," *Journal of Lightwave Technology*, vol. 33, no. 7, pp. 1445–1451, 2015.

[90] M. Karlsson and E. Agrell, "Spectrally efficient four-dimensional modulation," in *Optical Fiber Communications Conference (OFC)*, 2012.

[91] K. Onohara, T. Sugihara, Y. Miyata, K. Sugihara, K. Kubo, H. Yoshida, K. Koguchi, and T. Mizuochi, "Soft-decision forward error correction for 100 Gb/s digital coherent systems," *Optical Fiber Technology*, vol. 17, no. 5, pp. 452–455, 2011.

[92] A. Alvarado, E. Agrell, D. Lavery, R. Maher, and P. Bayvel, "Replacing the soft-decision FEC limit paradigm in the design of optical communication systems," *Journal of Lightwave Technology*, vol. 33, no. 20, pp. 4338–4352, 2015.

[93] A. Alvarado, T. Fehenberger, B. Chen, and F. M. Willems, "Achievable information rates for fiber optics: Applications and computations," *Journal of Lightwave Technology*, vol. 36, no. 2, pp. 424–439, 2018.

[94] U. Wachsmann, R. F. Fischer, and J. B. Huber, "Multilevel codes: Theoretical concepts and practical design rules," *IEEE Transactions on Information Theory*, vol. 45, no. 5, pp. 1361–1391, 1999.

[95] A. Alvarado and E. Agrell, "Four-dimensional coded modulation with bit-wise decoders for future optical communications," *Journal of Lightwave Technology*, vol. 33, no. 10, pp. 1993–2003, 2015.

[96] B. P. Smith and F. R. Kschischang, "A pragmatic coded modulation scheme for high-spectral-efficiency fiber-optic communications," *Journal of Lightwave Technology*, vol. 30, no. 13, pp. 2047–2053, 2012.

[97] T. Yoshida, A. Alvarado, M. Karlsson, and E. Agrell, "Post-FEC BER benchmarking for bit-interleaved coded modulation with probabilistic shaping," *Journal of Lightwave Technology*, vol. 38, no. 16, pp. 4292–4306, 2020.

[98] J. Cho and P. J. Winzer, "Probabilistic constellation shaping for optical fiber communications," *Journal of Lightwave Technology*, vol. 37, no. 6, pp. 1590–1607, 2019.

[99] P. J. Winzer, D. T. Neilson, and A. R. Chraplyvy, "Fiber-optic transmission and networking: the previous 20 and the next 20 years," *Optics Express*, vol. 26, no. 18, pp. 24 190–24 239, 2018.

[100] M. P. Yankov, D. Zibar, K. J. Larsen, L. P. Christensen, and S. Forchhammer, "Constellation shaping for fiber-optic channels with QAM and high spectral efficiency," *IEEE Photonics Technology Letters*, vol. 26, no. 23, pp. 2407–2410, 2014.

[101] R. F. Fischer, *Precoding and signal shaping for digital transmission.* John Wiley & Sons, 2005.

[102] T. M. Cover, *Elements of information theory.* John Wiley & Sons, 1999.

[103] G. D. Forney, Jr., R. G. Gallager, G. R. Lang, F. M. Longstaff, and S. U. Qureshi, "Efficient modulation for band-limited channels," *IEEE Journal on Selected Areas in Communications*, vol. 2, no. 5, pp. 632–647, 1984.

[104] K. Keykhosravi, G. Durisi, and E. Agrell, "Accuracy assessment of nondispersive optical perturbative models through capacity analysis," *Entropy*, vol. 21, no. 8, p. 760, 2019.

[105] H. Iimori, R.-A. Stoica, and G. T. F. de Abreu, "Constellation shaping for rate maximization in AWGN channels with non-linear distortion," in *International Workshop on Computational Advances in Multi-Sensor Adaptive Processing (CAMSAP)*, 2017.

[106] H. Iimori and G. T. F. de Abreu, "Rate-optimal communication under nonlinear Gaussian noise via constellation shaping," in *IEEE Wireless Communications and Networking Conference (WCNC)*, 2018.

[107] D. Pilori, F. Forghieri, and G. Bosco, "Maximization of the achievable mutual information using probabilistically shaped squared-QAM constellations," in *Optical Fiber Communication Conference (OFC)*, 2017.

[108] L. Schmalen, "Probabilistic constellation shaping: Challenges and opportunities for forward error correction," in *Optical Fiber Communications Conference (OFC)*, 2018.

[109] B. Chen, C. Okonkwo, H. Hafermann, and A. Alvarado, "Increasing achievable information rates via geometric shaping," in *European Conference on Optical Communication (ECOC)*, 2018.

[110] H. Krüger, B. Geiser, P. Vary, H. T. Li, and D. Zhang, "Gosset lattice spherical vector quantization with low complexity," in *International Conference on Acoustics, Speech and Signal Processing (ICASSP)*, 2011, pp. 485–488.

[111] H. Cohn, A. Kumar, S. Miller, D. Radchenko, and M. Viazovska, "The sphere packing problem in dimension 24," *Annals of Mathematics*, vol. 185, no. 3, pp. 1017–1033, 2017.

[112] G. D. Forney, Jr., "Multidimensional constellations-Part II. Voronoi constellations," *IEEE Journal on Selected Areas in Communications*, vol. 7, no. 6, pp. 941–958, 1989.

Included papers A–F

Paper A

"Lattice-based geometric shaping",
Ali Mirani, Erik Agrell, and Magnus Karlsson,
European Conference on Optical Communication (ECOC), Brussels, Belgium, Dec 2020.

Paper B

"Low-complexity geometric shaping",
Ali Mirani, Erik Agrell, and Magnus Karlsson,
Journal of Lightwave Technology, vol. 39, no. 2, pp. 363-371, Jan 2021.

Paper C

"Physical realizations of multidimensional Voronoi constellations in optical communication systems",
Ali Mirani, Kovendhan Vijayan, Shen Li, Zonglong He, Erik Agrell, Jochen Schröder, Peter Andrekson, and Magnus Karlsson,
submitted to *Journal of Lightwave Technology*, Nov 2022.

Paper D

"Capacity of phase-sensitively preamplified optical links at low signal-to-noise ratio",
Kovendhan Vijayan, **Ali Mirani**, Jochen Schröder, Magnus Karlsson, and Peter Andrekson,
European Conference on Optical Communication (ECOC), Basel, Switzerland, Sep 2022.

Paper E

"Comparison of uniform cross QAM and probabilistically shaped QAM formats under the impact of transmitter impairments",
Ali Mirani, Mikael Mazur, Erik Agrell, Benjamin Foo, Jochen Schröder, Peter Andrekson, and Magnus Karlsson,
European Conference on Optical Communication (ECOC), Dublin, Ireland, Sep 2019.

Paper F

"Performance of Probabilistic Shaping Coherent Channels in Hybrid Systems",
Diego Villafani, **Ali Mirani**, Henrik Åhlfeldt, Jochen Schröder, Magnus Karlsson, and Peter Andrekson,
International Conference on Transparent Optical Networks (ICTON), Bari, Italy, July 2020.